Received: 1 September 2016 | Accepted: 28 February 2017

DOI: 10.1111/jmg.12248

ORIGINAL ARTICLE

WILEY Journal of METAMORPHIC GEOLOGY

Fluid generation and evolution during exhumation of deeply subducted UHP continental crust: Petrogenesis of composite granite–quartz veins in the Sulu belt, China

S.-J. Wang[1,2] | L. Wang[1] | M. Brown[1,2] | P. M. Piccoli[2] | T. E. Johnson[3] | P. Feng[1] | H. Deng[1] | K. Kitajima[4] | Y. Huang[1]

[1]State Key Laboratory of Geological Processes and Mineral Resources and Center for Global Tectonics, School of Earth Sciences, China University of Geosciences, Wuhan, China

[2]Laboratory for Crustal Petrology, Department of Geology, University of Maryland, College Park, MD, USA

[3]Department of Applied Geology, The Institute for Geoscience Research (TIGeR), Curtin University, Perth, WA, Australia

[4]The WiscSIMS Laboratory, Department of Geoscience, University of Wisconsin-Madison, Madison, WI, USA

Correspondence
Lu Wang, State Key Laboratory of Geological Processes and Mineral Resources, and Center for Global Tectonics, School of Earth Sciences, China University of Geosciences, Wuhan, China.
Email: wanglu@cug.edu.cn

Funding information
National Natural Science Foundation of China, Grant/Award Number: 41272225, 41572182; China Scholarship Council, Grant/Award Number: 201506410003; Fundamental Research Funds for National University; China University of Geosciences, Grant/Award Number: CUG–G1323511572; US National Science Foundation, Grant/Award Number: EAR03-19230, EAR10-53466, EAR13-55590

Submitting editor: Katy Evans

Abstract

Composite granite–quartz veins occur in retrogressed ultrahigh pressure (UHP) eclogite enclosed in gneiss at General's Hill in the central Sulu belt, eastern China. The granite in the veins has a high-pressure (HP) mineral assemblage of dominantly quartz+phengite+allanite/epidote+garnet that yields pressures of 2.5–2.1 GPa (Si-in-phengite barometry) and temperatures of 850–780°C (Ti-in-zircon thermometry) at 2.5 GPa (~20°C lower at 2.1 GPa). Zircon overgrowths on inherited cores and new grains of zircon from both components of the composite veins crystallized at *c.* 221 Ma. This age overlaps the timing of HP retrograde recrystallization dated at 225–215 Ma from multiple localities in the Sulu belt, consistent with the HP conditions retrieved from the granite. The $\varepsilon_{Hf}(t)$ values of new zircon from both components of the composite veins and the Sr–Nd isotope compositions of the granite consistently lie between values for gneiss and eclogite, whereas $\delta^{18}O$ values of new zircon are similar in the veins and the crustal rocks. These data are consistent with zircon growth from a blended fluid generated internally within the gneiss and the eclogite, without any ingress of fluid from an external source. However, at the peak metamorphic pressure, which could have reached 7 GPa, the rocks were likely fluid absent. During initial exhumation under UHP conditions, exsolution of H_2O from nominally anhydrous minerals generated a grain boundary supercritical fluid in both gneiss and eclogite. As exhumation progressed, the volume of fluid increased allowing it to migrate by diffusing porous flow from grain boundaries into channels and drain from the dominant gneiss through the subordinate eclogite. This produced a blended fluid intermediate in its isotope composition between the two end-members, as recorded by the composite veins. During exhumation from UHP (coesite) eclogite to HP (quartz) eclogite facies conditions, the supercritical fluid evolved by dissolution of the silicate mineral matrix, becoming increasingly solute-rich, more 'granitic' and more viscous until it became trapped. As crystallization began by diffusive loss of H_2O to the host eclogite concomitant with ongoing exhumation of the crust, the trapped supercritical fluid intersected the solvus for the granite–H_2O system, allowing phase separation and formation of the composite granite–quartz veins. Subsequently, during the transition from HP eclogite to amphibolite facies conditions, minor phengite breakdown melting is recorded in both the

granite and the gneiss by K-feldspar+plagioclase+biotite aggregates located around phengite and by K-feldspar veinlets along grain boundaries. Phase equilibria modelling of the granite indicates that this late-stage melting records *P–T* conditions towards the end of the exhumation, with the subsolidus assemblage yielding 0.7–1.1 GPa at <670°C. Thus, the composite granite–quartz veins represent a rare example of a natural system recording how the fluid phase evolved during exhumation of continental crust. The successive availability of different fluid phases attending retrograde metamorphism from UHP eclogite to amphibolite facies conditions will affect the transport of trace elements through the continental crust and the role of these fluids as metasomatic agents interacting with the mantle wedge in the subduction channel.

KEYWORDS

composite granite–quartz veins, hydrous melt/aqueous fluid immiscibility, phase equilibria modelling, Sulu belt, supercritical fluid, UHP/HP eclogite

1 | INTRODUCTION

Aqueous fluid, supercritical fluid and hydrous melt exert an important influence on the composition and physical properties of their host rocks. Large-scale flow of these fluids in subduction zones drives element recycling and mass and heat transfer, leading to substantial crust–mantle interactions and arc magmatism (Bebout, 2014; Bebout & Penniston-Dorland, 2016; Brown, Korhonen, & Siddoway, 2011; Brown & Rushmer, 2006; Keppler, 2017; Kessel, Schmidt, Ulmer, & Pettke, 2005; Manning, 2004; Spandler & Pirard, 2013; Zheng, 2012). In addition, the liberation of fluid or melt during subduction may cause rheological weakening of the lithosphere, which may facilitate exhumation of subducted continental crust from high and ultrahigh pressure (HP–UHP) metamorphic conditions (e.g. Ferrero, Wunder, Walczak, O'Brien, & Ziemann, 2015; Gerya & Meilick, 2011; Labrousse, Duretz, & Gerya, 2015; Labrousse, Prouteau, & Ganzhorn, 2011; Rosenberg & Handy, 2005; Sizova, Gerya, & Brown, 2012).

Recent research into the fluid regime associated with subduction has focused on the possibility of hydrous melt–aqueous fluid supercriticality at UHP conditions (e.g. Mibe, Kawamoto, Matsukage, Fei, & Ono, 2011; Zheng & Hermann, 2014; Zheng, Xia, Chen, & Gao, 2011). Under most conditions supercritical fluid and hydrous melt have a greater capacity than aqueous fluid to transport trace elements (Hayden & Manning, 2011; Hermann & Rubatto, 2014; Schmidt & Poli, 2014; Sheng, Zheng, Li, & Hu, 2013), except close to the critical curves for silicate–H_2O systems (Keppler, 2017). Indeed, supercritical fluid is increasingly argued to be the principal phase migrating from the subducting slab into the overlying mantle wedge deep beneath arcs, where it may separate during ascent into two immiscible phases—hydrous melt and aqueous fluid (e.g. Kawamoto, Kanzaki, Mibe, Matsukage, & Ono, 2012; Kawamoto et al., 2014; Liu et al., 2014). Similarly, during exhumation of deeply subducted continental crust, a synmetamorphic supercritical fluid may separate into hydrous melt and aqueous fluid potentially leading to the precipitation of mineral deposits and/or complex vein systems (Hack, Thompson, & Aerts, 2007; Zheng & Hermann, 2014; Zheng et al., 2011). To understand these fluid-related processes operating during deep subduction, it is important to characterize evidence of the generation and subsequent evolution of fluids as recorded by UHP metamorphic rocks preserved along intra-continental sutures, which represent sites of former continental subduction (e.g. Brown, 2014; Liou, Ernst, Zhang, Tsujimori, & Jahn, 2009; Schertl & O'Brien, 2013).

The Sulu belt in eastern China is a well-studied example of continental crust that has been subducted to mantle depths. The Sulu belt reached peak *P–T* conditions generally exceeding 3.5–4.5 GPa at 700–850°C (e.g. Liu, Gerdes, Liou, Xue, & Liang, 2006; Wang, Wang, Brown, & Feng, 2016; Wang et al., 2014; Zhang, Xiao, Hoefs, Liou, & Simon, 2006), and may have reached pressures as high as 7 GPa at 1,000°C (Ye, Cong, & Ye, 2000). At these *P–T* conditions any remaining prograde synmetamorphic fluid will have been supercritical, which is consistent with the occurrence of multiphase solid inclusions interpreted to have precipitated from supercritical fluid trapped in UHP garnet and kyanite (e.g. Ferrando, Frezzotti, Dallai, & Compagnoni, 2005; Frezzotti, Ferrando, Dallai, & Compagnoni, 2007; Wang et al., 2016). Accordingly, the Sulu belt provides an opportunity to investigate the evolution of fluid attending retrograde metamorphism during exhumation from UHP conditions.

2 | FLUIDS AND HP–UHP METAMORPHISM

2.1 | Phase relations in silicate–H_2O systems

In silicate–H_2O systems, experimental studies have shown that the fluid phase attending metamorphism varies widely in composition and properties with *P–T* (Figure 1). In particular, although aqueous fluid and hydrous melt are immiscible at low pressures they form a single miscible phase at pressures above the second critical endpoint (SCE), which is where the solvus between fluid and melt closes and a solidus may no longer be distinguished (Hack et al., 2007; Hermann, Spandler, Hack, & Korsakov, 2006). The SCEs for granite and basalt are located at ~2.2–3.0 GPa/630–680°C (range for haplogranite to Ca-bearing granite, Hack et al., 2007) and 3.4 GPa/770°C (Mibe et al., 2011), respectively.

At temperatures lower than the SCE and the wet solidus, the phase in equilibrium with silicate minerals is an aqueous fluid in which dissolved solutes increase with increasing pressure (Figure 1). By contrast, at temperatures above the wet solidus, but at pressures below the critical curve—the locus of points where the hydrous melt+aqueous fluid solvus closes, which extends from the SCE to higher temperatures and lower pressures with changing solute content in silicate–H_2O systems (Figure 1; Hack et al., 2007; Hermann et al., 2006)—two immiscible phases may be in equilibrium with silicate minerals, both an aqueous fluid and a hydrous melt (Figure 1). In nature, unless the system is oversaturated with H_2O, with increasing temperature below the critical curve excess H_2O progressively dissolves into the melt until no free aqueous fluid remains at high temperatures. With increasing pressure at suprasolidus conditions, aqueous fluid and hydrous melt form a supercritical fluid at pressures above the critical curve (Figure 1).

Hermann et al. (2006) argued that aqueous fluid and hydrous melt are compositionally well defined, and that there is only a narrow range of temperatures above the SCE (<100°C) where transitional solute-rich fluid exists. Accordingly, they proposed that fluids with <30 wt% solutes be called aqueous, those with >65 wt% solutes be called hydrous melts, and those with intermediate compositions be called transitional supercritical fluids. However, as discussed by Frezzotti and Ferrando (2015), there are arguments against using an arbitrary concentration of solute to subdivide a supercritical fluid from a hydrous melt at pressures above the SCE and the critical curve. In this study, although we follow the recommendation by Hermann et al. (2006) to separate aqueous fluid from supercritical fluid at 30 wt% solute, as solute concentration increases with temperature at pressures above the critical curve we do not arbitrarily distinguish two separate phases within this continuum, but refer to all compositions with >30 wt% solute as supercritical fluid (Figure 1). We acknowledge that with decreasing pressure and increasing temperature along the critical curve solute content increases from ~65 wt% at the SCE to ~95 wt% at 900°C, and the supercritical fluid increasingly has properties similar to those of melt with, for example, a fivefold increase in viscosity (Audétat & Keppler, 2004; Hack & Thompson, 2011).

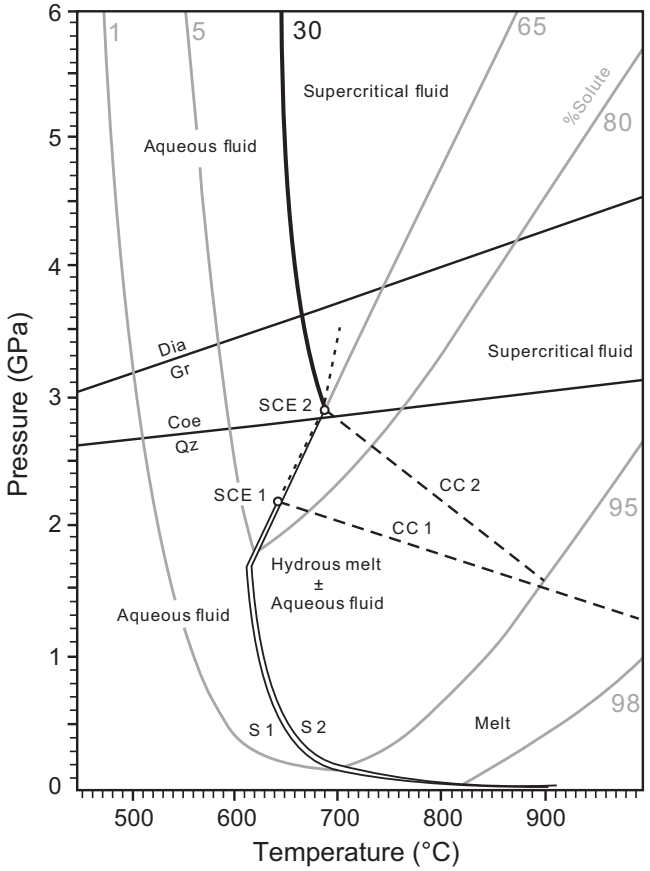

FIGURE 1 *P–T* phase diagram for silicate–H_2O systems. The wet solidi for haplogranite (no CaO; S 1) and granite (CaO of 1.93 wt%, plagioclase An_{20}; S 2) terminate at inferred second critical endpoints (SCE 1 and SCE 2) that vary with composition; the critical curves (the locus of points where the hydrous melt+aqueous fluid solvus closes) for haplogranite (CC 1) and granite (CC 2) extend from the SCEs down pressure and converge with increasing temperature (from Hack et al., 2007). The uncertainty on the pressure of the critical curves is ±0.2 GPa (Bureau & Keppler, 1999). The gray lines are isopleths of wt% solute in the fluid phase (Hermann et al., 2006, 2013). The *P–T* fields for aqueous fluid (at lower temperatures), immiscible hydrous melt+aqueous fluid (at intermediate temperatures and lower pressures), melt (at higher temperatures and lower pressures) and supercritical fluid (at higher pressures), all in equilibrium with silicate minerals, are shown

2.2 | Origin of fluids in exhuming continental crust

Normally there is continuous release and loss of fluid during progressive metamorphism. Ultimately, this process may lead to fluid absent conditions at the highest pressures and temperatures in the eclogite and granulite facies (Yardley & Valley, 1997), which may inhibit complete equilibration prior to peak *P–T* conditions (e.g. Young & Kylander-Clark, 2015). If rocks become fluid absent prior to peak pressure, what is the origin of fluids associated with retrogression during exhumation of UHP metamorphic rocks?

Multiple studies have shown that a large amount of H_2O may be stored in the continental crust in nominally anhydrous minerals (NAMs) as structural hydroxyl in point defects in the crystal lattice and as molecular water in clusters of molecules (Xia, Sheng, Yang, & Yu, 2005; Zheng, 2009). For example, the H_2O concentrations in garnet and omphacite from UHP eclogite in the Dabie–Sulu orogen are 1,000–3,000 ppm (reviewed by Zheng, 2009), and the total whole-rock H_2O content for phengite-free eclogite is ~2,500 ppm (Chen, Zheng, & Gong, 2011). Similarly, the H_2O concentrations in quartz, plagioclase and K-feldspar from UHP gneiss in the southern Sulu belt are 1,500–3,500 ppm, and the total whole-rock H_2O content for one hydrate-free gneiss is ~2,400 ppm (Chen, Zheng, & Gong, 2011). More recently, Gong, Chen, and Zheng (2013) suggested that the highest total H_2O contents of NAMs in eclogite at Yangkou (2,500 ppm in garnet and 3,500 ppm in omphacite), ~2 km to the north of the study area, provide a minimum estimate of the total H_2O content under UHP conditions. Addition of phengite, epidote, biotite or amphibole to the mineral assemblage increases the whole-rock H_2O content considerably, in proportion to the mode of these hydrous minerals. Plausibly, up to 1 wt% H_2O, maybe more in some circumstances, could be stored in UHP eclogite at peak conditions.

Experimental studies have demonstrated increasing solubility of H_2O in NAMs with increasing pressure, potentially leaving little or no free fluid at the peak of UHP metamorphism (reviewed by Zheng, 2009). The converse of this relationship is the decreasing solubility of H_2O in NAMs with decreasing pressure, leading to exsolution of molecular H_2O and hydroxyl from NAMs during exhumation. In addition, the hydroxyl in hydrous minerals in eclogite has been argued to facilitate destabilization of omphacite to form symplectite without any requirement of fluid infiltration (Martin & Duchêne, 2015). Thus, continental crust metamorphosed at UHP conditions stores H_2O in NAMs and hydrous minerals that will be made available during exhumation, providing an internal source of fluids considered sufficient to facilitate retrogression (Chen, Zheng, & Gong, 2011; Zheng, 2009).

2.3 | Evidence of fluids in exhumed continental crust

As reviewed in Table S1, although evidence of a grain-scale supercritical fluid accompanying the late prograde to peak stage of UHP metamorphism has been presented from several orogenic belts (e.g. Ferrando, Frezzotti, Petrelli, & Compagnoni, 2009; Ferrando et al., 2005; Malaspina, Scambelluri, Poli, van Roermund, & Langenhorst, 2010; Scambelluri, Pettke, & van Roermund, 2008; Stöckhert, Duyster, Trepmann, & Massonne, 2001; Stöckhert, Trepmann, & Massonne, 2009; van Roermund, Carswell, Drury, & Heijboer, 2002; Vrijmoed, Smith, & van Roermund, 2008), our knowledge of the origin and subsequent evolution of supercritical fluid during the retrograde evolution of rocks is limited (Frezzotti & Ferrando, 2015; Hack et al., 2007; Xia, Zheng, & Hu, 2010). One issue in identifying the former presence of a supercritical fluid in exhumed UHP crust is the changing composition of the fluid across the range of *P–T* conditions (Frezzotti & Ferrando, 2015; Hack et al., 2007; Hermann, Zheng, & Rubatto, 2013; Schmidt & Poli, 2014). As a result, precipitates from a supercritical fluid at pressures above the critical curve have a wide range of possible compositions, which may make distinguishing them from the products of hydrous melts at pressures below the critical curve challenging (Frezzotti & Ferrando, 2015). Studies of multiphase solid inclusions trapped under UHP conditions (i.e. above the critical curves for silicate–H_2O systems) suggest that compositions of supercritical fluids typically are high in fluid-mobile element contents, such as K, Na, LREE (light rare earth elements) and LILE (large ion lithophile elements), and also HREE (heavy rare earth elements), HFSE (high field strength elements) and transition metals (Table S1). However, caution is necessary since multiphase solid inclusions in UHP metamorphic rocks may represent an incomplete record or they may have been modified in composition during exhumation (Hermann & Rubatto, 2014; Hermann et al., 2013). In addition, the small size and variable composition (Gao, Zheng, Chen, & Hu, 2013) of multiphase solid inclusions, which are generally only tens of microns in diameter, limits the information we can obtain from them concerning the parent fluids, particularly with respect to the source of the fluids and the timing of fluid availability.

The most visible evidence of channelized fluid flow during subduction and exhumation is represented by HP–UHP vein systems that are common in eclogite facies metamorphic rocks (Gao & Klemd, 2001; Guo et al., 2015; Rubatto & Hermann, 2003; Spandler & Hermann, 2006; Spandler, Pettke, & Rubatto, 2011; Zhang et al., 2008). These systems register information useful in deciphering the evolution of fluids attending metamorphism.

Here, we present the results of a study of a coastal outcrop in the central Sulu belt, where composite granite–quartz veins occur within eclogite blocks enclosed in the volumetrically dominant gneisses, which together comprise the subducted leading edge of the Yangtze Craton. We integrate observations from field relationships and petrography, with mineral and whole-rock compositions, including Sr–Nd isotopes, zircon U–Pb geochronology and Hf–O isotopes, and thermobarometry and phase equilibria modelling to develop a comprehensive understanding of the origin and source of fluid after the UHP metamorphic peak and its evolution during exhumation.

3 | GEOLOGICAL SETTING

The Dabie–Sulu orogen in central–eastern China marks the site of northward subduction and collision of the Yangtze Craton beneath the North China Craton during the Triassic (Figure S1a; e.g. Ernst, Tsujimori, Zhang, & Liou, 2007; Liou, Zhang, Liu, Zhang, & Ernst, 2012). At the eastern end of the orogen, the Sulu belt was displaced to the northeast by ~500 km of sinistral offset along the NNE-trending Tan–Lu fault. Based on integrated field, petrological and geochemical studies, the Sulu belt is divided into a southern HP and a central and northern UHP zone (Liu, Xu, & Liou, 2004; Xu et al., 2006). The UHP zone consists of mainly orthogneiss and paragneiss, with minor eclogite, garnet peridotite, quartzite and marble, all of which are intruded by post-orogenic granites (Hacker et al., 2000; Zhang, Liou, & Ernst, 2009). Eclogite occurs as blocks and lenses enclosed mainly in gneisses, but sometimes in garnet peridotite and marble. Coesite occurs in eclogite and as inclusions in zircon from eclogite, quartzite and gneiss (e.g. Chen, Zheng, & Hu, 2013; Liu & Liou, 2011; Ye, Yao, et al., 2000; Zhang, Liou, & Ernst, 1995). SHRIMP U–Pb dating of coesite-bearing domains in zircon from these rocks has yielded metamorphic ages from 234 ± 4 Ma to 225 ± 2 Ma (Liu & Liou, 2011), indicating that all these units record the Triassic UHP metamorphism.

This study area is located in the central Sulu belt at General's Hill (Figure S1b), ~35 km northeast of Qingdao, where a continuous outcrop 50–100 m wide extends along the coast for ~1 km (the northern part of the outcrop is shown in Figure 2). The outcrop consists of strongly foliated, tight to isoclinally folded migmatitic eclogite striking SSE–NNW with moderate to steep dips to the WSW (Figure 2). The eclogite hosts foliation-parallel centimetre-scale stromatic leucosomes and metre-scale sheets of leucosome spaced a few to several tens of metres apart and interpreted to be former melt ascent channels (Wang et al., 2014). The leucosome is moderately to strongly foliated, with the foliation mainly defined by phengite, elongated quartz and feldspar. The migmatitic eclogite is surrounded by felsic gneiss and the outcrop is cut by quartz and feldspar porphyry dykes.

Based on structural mapping, and petrological and geochemical analysis, the migmatitic eclogite has been argued to record successive stages of generation and migration of melt derived from the UHP eclogite by phengite-breakdown melting during exhumation (Wang et al., 2014). LA-ICP-MS U–Pb dating of zircon overgrowths from leucosome, retrogressed eclogite and migmatite yielded weighted mean $^{206}Pb/^{238}U$ ages (±2σ) of 228 ± 6 Ma, 224 ± 4 Ma and 219 ± 5 Ma (Wang et al., 2014). The peak of UHP metamorphism has been dated at *c.* 233 Ma at Yangkou, ~2 km to the north of General's Hill (Figure S1; Zeng, Gao, Yu, & Hu, 2011). These ages indicate that melt crystallization occurred during exhumation of the Sulu belt.

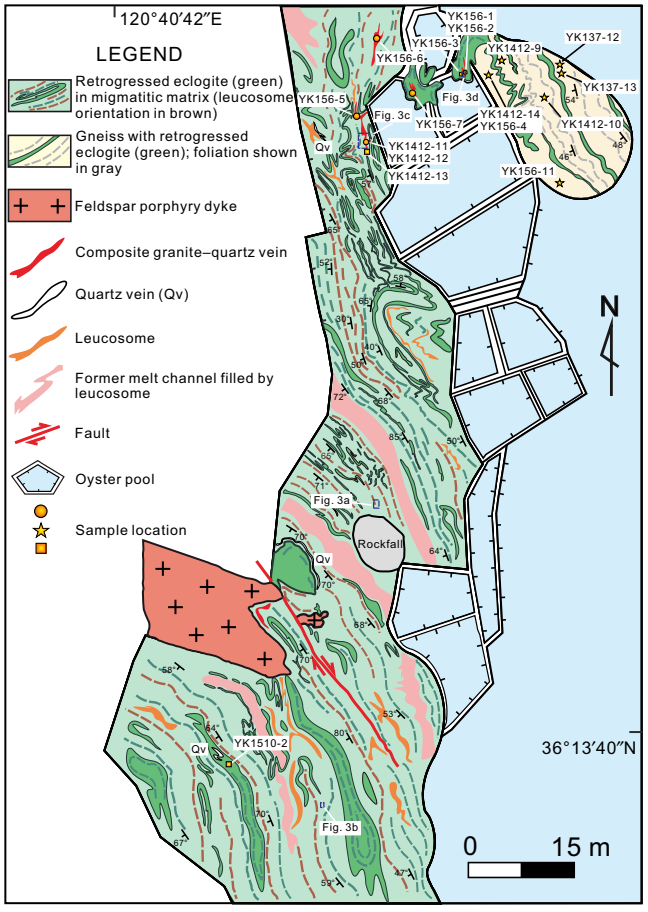

FIGURE 2 Geological map of the coastal outcrop at General's Hill, with sample locations marked in solid circles, squares and stars representing composite granite–quartz veins, the host eclogite and the surrounding gneiss, respectively (detailed map based on the regional mapping of Wang et al., 2014). For location of the General's Hill outcrop in relation to the Sulu belt as a whole, see Figure S1

In this study, the regional mapping of Wang et al. (2014) was supplemented by 1:500 scale structural mapping that targeted centimetre- to decimetre-scale composite granite–quartz veins in the northern part of the outcrop adjacent to the enclosing gneiss (Figure 2). The host eclogite is fine-grained and variably retrogressed, while the enclosing gneiss is compositionally homogeneous, with a weak foliation that is gently folded. The composite veins have sharp contacts with the host eclogite, with the quartz commonly separating granite from host eclogite (Figure 3c, d), and are generally oriented parallel to the foliation, although many have irregular margins (Figure 3b,c). Centimetric enclaves of eclogite in the composite veins are consistent with an intrusive origin (Figure 3a,b).

Seventeen samples were collected at General's Hill, as summarized in Table S2 and illustrated in Figures 2 and 3, including two sets of granite–quartz samples from composite veins (YK1412-12 and YK1412-11; YK156-2 and YK156-1), the local host retrogressed eclogite (YK1412-13, YK156-3) and the adjacent gneiss (YK1412-14; YK156-4). Three other granite samples from composite veins (YK156-5, -6, -7), one additional eclogite (YK1510-2) and five other gneisses (YK137-12, -13, YK1412-9, -10, YK156-11) were sampled. Details of all analytical methods are provided in Appendix S1.

4 | RESULTS

4.1 | Petrography

In the composite veins, the granite is composed of quartz (45–49 vol.%)+phengite (22–30 vol.%)+allanite/epidote (3–10 vol.%)+rare garnet, with plagioclase (5–13 vol.%)+K-feldspar (6–11 vol.%), minor biotite (replacing phengite)

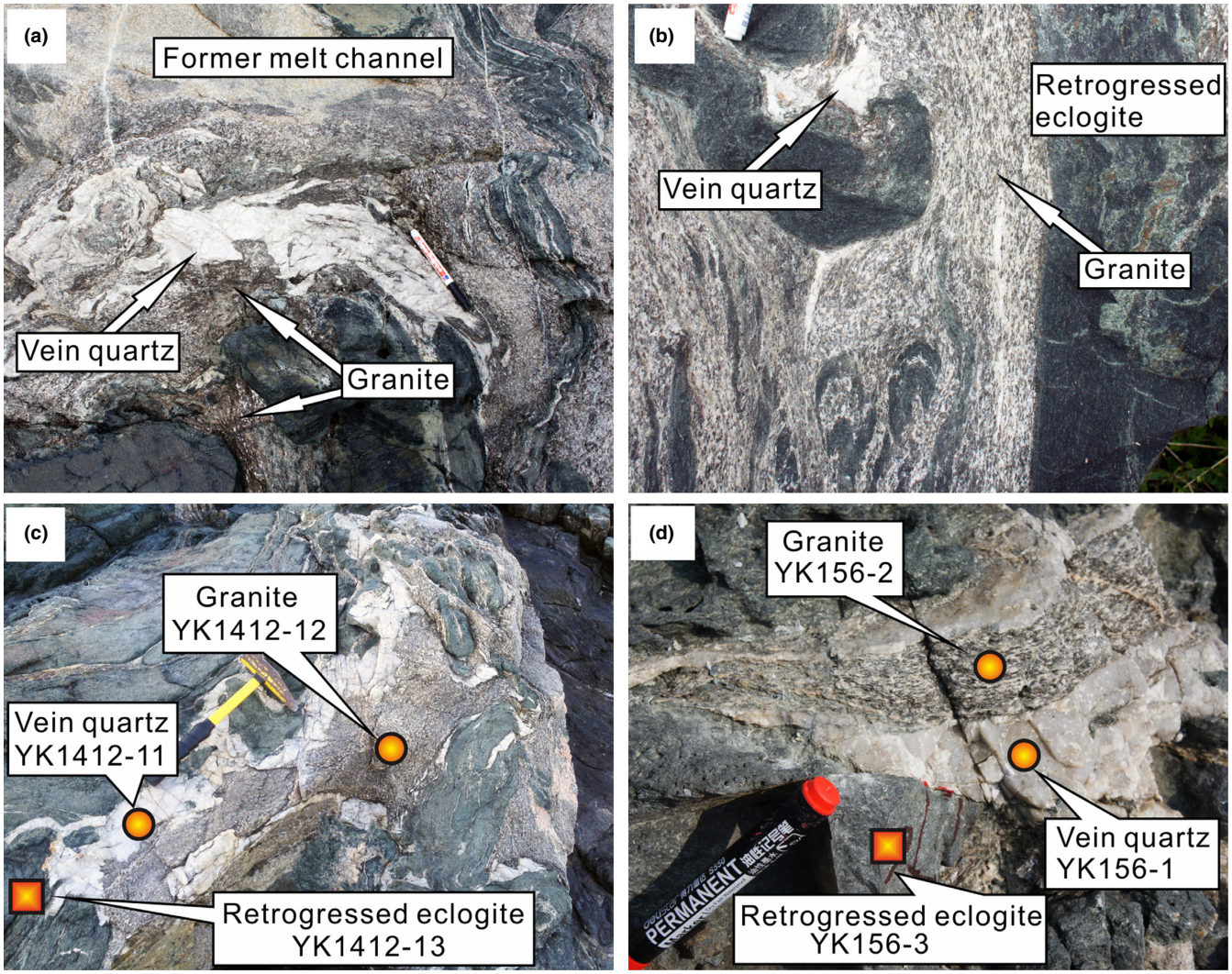

FIGURE 3 Field occurrence of the composite granite–quartz veins at General's Hill (a–d), with sample locations marked in (c) and (d); in (b), the granite contains small enclaves of partially assimilated retrogressed eclogite. The composite veins are centimetre to decimetre in width and emplaced into retrogressed eclogite

and hornblende (replacing garnet), and scarce apatite, zircon, rutile with thin rims of ilmenite (in phengite), and titanite (Figure 4a–d). Phengite has 3.40–3.29 Si per formula unit (pfu; Table S3a, one analysis with 3.25 Si pfu). At the edges, phengite is surrounded by aggregates of variable thickness composed of biotite+plagioclase+K-feldspar from which thin films, cuspate veinlets and patches of K-feldspar with low dihedral angles extend along grain boundaries (Figure 4e–i). Plagioclase occurs primarily in symplectites after phengite and garnet, and only occasionally as subhedral grains (Figure 4b,c), distinguishing the granite from the gneiss (Figure 5c,e). Garnet occurs as either subhedral grains showing minor retrogression or as relict fragments within symplectites of hornblende+plagioclase+opaque oxide (Figure 4c). Millimetre-sized euhedral–subhedral epidote grains commonly have allanite cores (Figure 4d); in addition, they contain fine-grained inclusions of quartz, apatite and zircon (e.g. Figure 4d). By contrast, the vein quartz in the composite veins is almost entirely composed of anhedral quartz (>99 vol.%), with only rare biotite and zircon.

The host eclogite is strongly foliated with extensive amphibolite facies retrogression, where garnet, omphacite and phengite are almost entirely replaced by various symplectites (Figure 5a,b). The symplectites comprise either hornblende+plagioclase after omphacite, or hornblende+plagioclase+opaque oxide after garnet, or biotite+plagioclase after phengite, and occur within a matrix of fine-grained garnet, hornblende, quartz, apatite, zircon and rutile/ilmenite (Figure 5a,b).

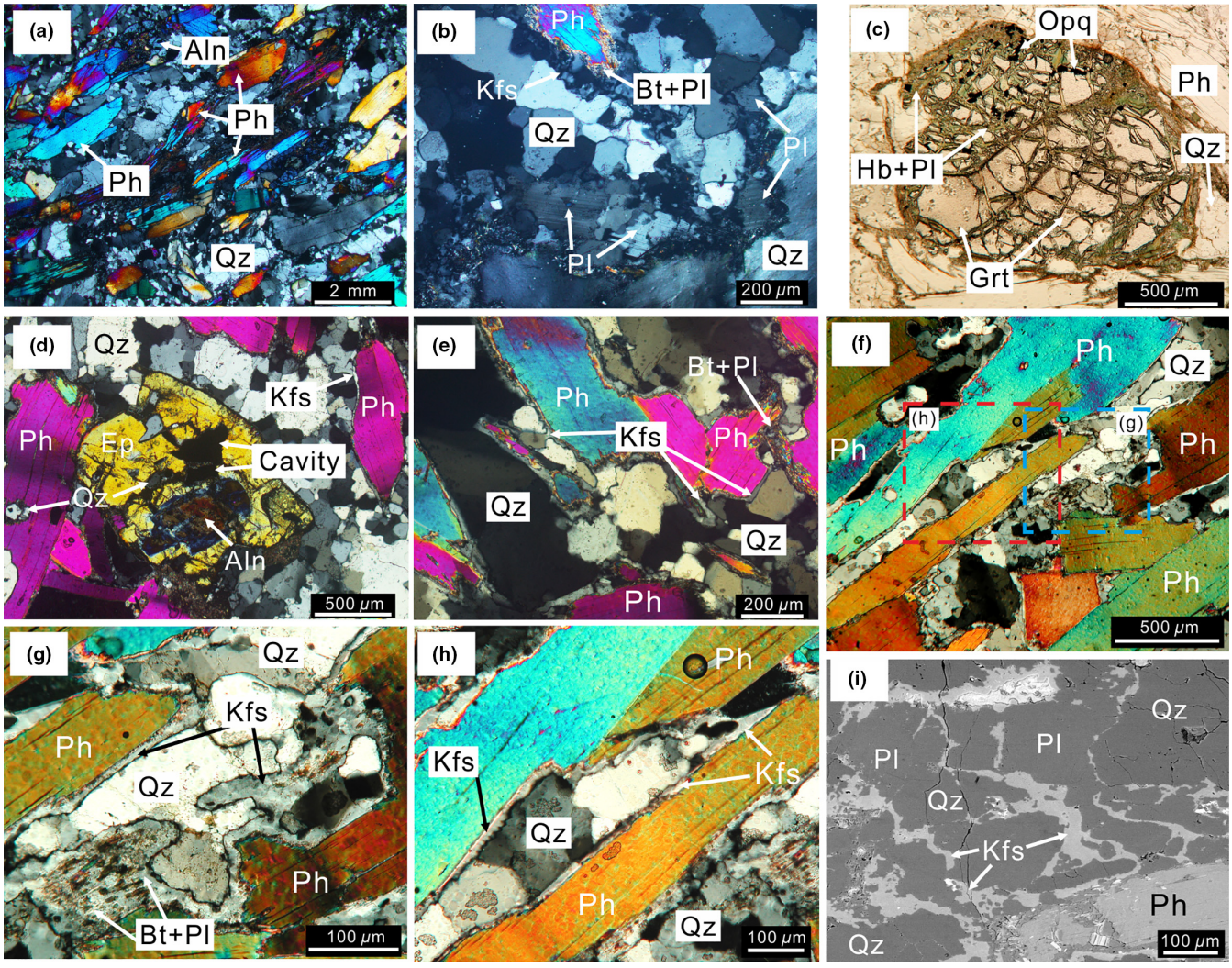

FIGURE 4 Representative photomicrographs to show the mineralogy and microstructures of the granite in the composite veins. (a–d) Images to show the main mineral assemblage of Qz+Ph+Pl+Grt+Aln/Ep+Kfs (a, b, d in cross-polarized light and c in plane-polarized light). Garnet mostly occurs as relict grains surrounded by Hb+Pl+Opq symplectite (c); allanite and epidote exhibit distinct core–rim structure (d). (e–i) Images to show the occurrence of K-feldspar as interstitial cuspate veinlets and films with low dihedral angles along grain boundaries of phengite and quartz (e–h in cross-polarized light and i backscattered electrons). Mineral names are abbreviated according to Whitney and Evans (2010)

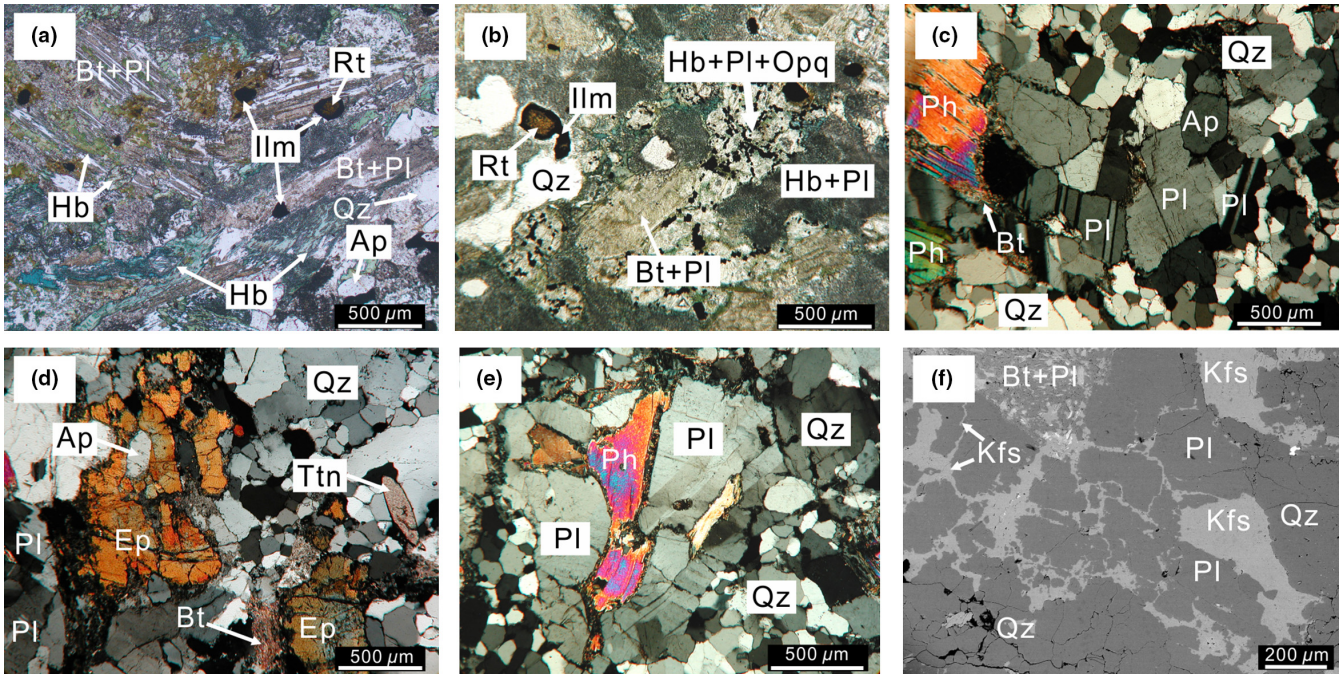

FIGURE 5 Representative images to show mineralogy and microstructures of retrogressed eclogite; (a, b) and gneiss (c–f). (a, b) Retrogressed eclogite showing the mineral assemblage of Hb+Qz+Ap+Grt+Rt/Ilm and Hb+Pl symplectite after Omp, Hb+Pl+Opq symplectite after Grt and Bt+Pl symplectite after Ph; rutile is mostly retrogressed to ilmenite at the rim (plane-polarized light). (c–e) Gneiss showing the mineral assemblage of Qz+Pl+Kfs+Ph+Aln/Ep+Ttn; phengite is retrogressed to Bt+Pl+Kfs at the edges (cross-polarized light). (f) In addition to subhedral grains, Kfs also occurs as cuspate veinlets and patches along grain boundaries of plagioclase and quartz (backscattered electrons). Mineral names are abbreviated according to Whitney and Evans (2010)

The gneiss consists of quartz (44–48 vol.%)+plagioclase+(30–38 vol.%)+K-feldspar (10–16 vol.%)+phengite (5–7 vol.%)+allanite/epidote (<1 vol.%) with accessory zircon, titanite and apatite (Figure 5c–f); unlike the granite, the gneiss does not contain garnet. Coarse phengite is retrogressed to biotite+plagioclase+K-feldspar at the edges (Figure 5c,e,f). Allanite and epidote form anhedral grains up to 1 mm in diameter, and contain inclusions including apatite, quartz and zircon (e.g. Figure 5d). By contrast with the granite in the composite veins, in the gneiss some subhedral plagioclase grains have retained their primary magmatic features, such as multiple twinning and larger grain size (up to several mm; Figure 5c,e). K-feldspar occurs as subhedral grains, and also as cuspate veinlets along grain boundaries between plagioclase and quartz (Figure 5f). Large quartz grains exhibit subgrain formation, otherwise quartz forms the major phase with minor feldspar in a finer-grained, anastomosing matrix, where it exhibits granoblastic–polygonal microstructure.

4.2 | Whole-rock major and trace element compositions

The major and trace element compositions of the composite granite–quartz veins, the host eclogites and the surrounding gneisses are summarized in Table S3b, and Figures S2 and 6. The granites in the veins have high SiO_2 (73.01–75.39 wt%), K_2O (3.79–4.26 wt%), Ba (1,478–1,816 ppm) and Sr (786–2,076 ppm), but low Na_2O (0.99–1.35 wt%), FeO_t (1.44–2.43 wt%) and MgO (0.52–1.14 wt%). They are characterized by high REE contents ($\sum$REE = 170–276 ppm), and on a chondrite-normalized plot show enriched LREE and flat HREE patterns [$(La/Yb)_N$ = 21.80–42.26; $(Gd/Yb)_N$ = 2.02–3.39; Figure 6a] with weakly negative to negligible Eu anomalies (Eu/Eu* = 0.74–0.91). In a primitive mantle-normalized multi-element diagram (Figure 6b), the granite shows enrichment in LILE, notably Sr, but a moderate depletion in HFSE, including Nb and Ta.

The vein quartz of the composite veins has 99.10 wt% SiO_2 and very low abundances of all other oxides, reflecting the dominance of modal quartz. The sample also has low concentrations of all trace elements. It is characterized by a relatively flat chondrite-normalized REE pattern [$(La/Yb)_N$ = 14.56; Figure 6a], with slight LREE enrichment [$(La/Sm)_N$ = 8.39] and a moderately negative Eu anomaly (Eu/Eu* = 0.33). In a primitive mantle-normalized multi-element diagram (Figure 6b), the sample shows weak depletion of Nb and Sr with a significant positive anomaly for Pb.

The host eclogites contain moderate SiO_2 (49.09–54.34 wt%) and MgO (4.72–5.07 wt%), but high FeO_t

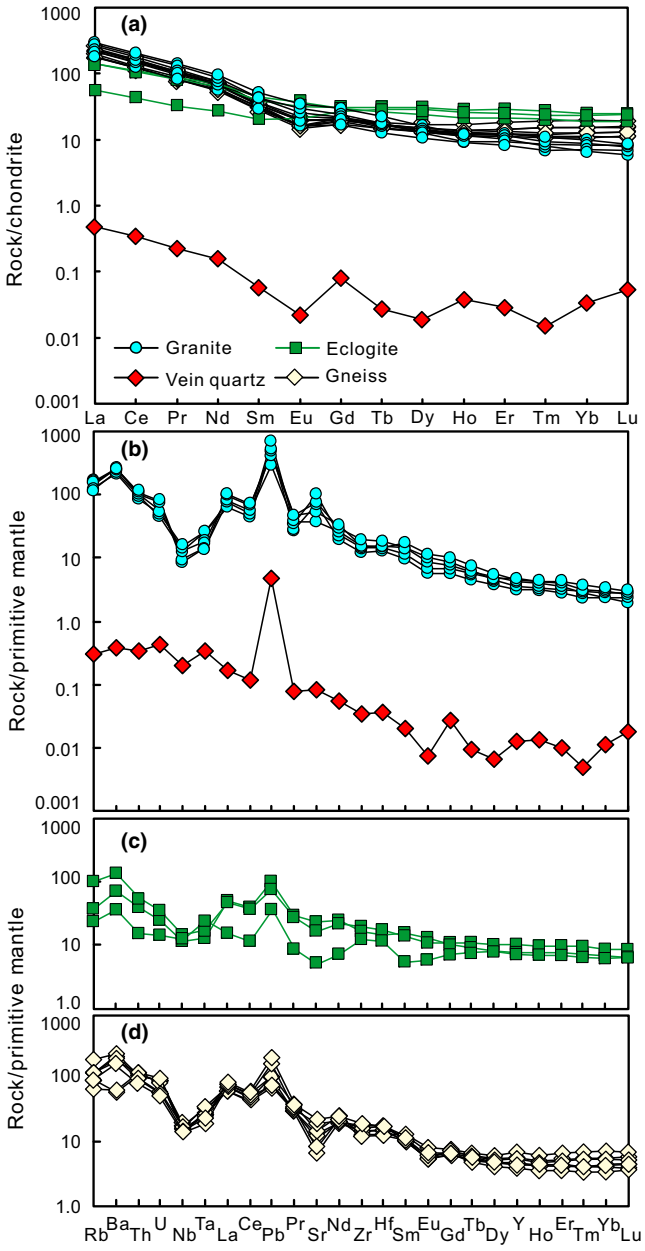

FIGURE 6 Whole-rock chondrite-normalized rare earth element patterns (a) and primitive mantle-normalized trace element patterns (b–d) of the granite and vein quartz from the composite veins (a, b), the host eclogites (a, c) and the surrounding gneisses (a, d). Normalization values are from Sun and McDonough (1989)

(9.15–13.10 wt%) and Na_2O (3.30–4.79 wt%) contents. They have moderate REE abundances ($\sum$REE = 85–173 ppm) and exhibit mildly enriched to flat chondrite-normalized LREE [$(La/Sm)_N$ = 2.82–3.56] and flat HREE [$(Gd/Yb)_N$ = 1.16–1.56] patterns with negligible Eu anomalies (Eu/Eu* = 0.90–1.00; Figure 6a). In a primitive mantle-normalized multi-element diagram, the eclogites are generally enriched in HFSE and LILE such as Zr, Hf and Ba (Figure 6c).

The gneisses have high SiO_2 (69.70–74.92 wt%), Na_2O (3.48–4.94 wt%) and K_2O (2.11–4.83 wt%) contents. In contrast to the granite in the composite veins, they have higher Na_2O and Yb, and lower Sr (Figure S2a,b). The gneisses also have high REE concentrations ($\sum$REE = 167–222 ppm), and in chondrite-normalized REE plot are seen to be enriched in LREE and have flat HREE patterns [$(La/Yb)_N$ = 11.58–22.69; $(Gd/Yb)_N$ = 1.07–1.96] with slightly negative Eu anomalies (Eu/Eu* = 0.62–0.81; Figure 6a). In a primitive mantle-normalized multi-element diagram, the gneisses are depleted in Nb, Ta, Sr and enriched in Th, U and Pb (Figure 6d). The high Na_2O and low Sr contents distinguish the gneiss from the granite in the composite veins (Figure S2).

4.3 | Whole-rock Sr–Nd isotopes

The whole-rock Sr–Nd isotope compositions of granite from the composite veins, the host eclogites and the surrounding gneisses are given in Table S4 and shown in Figure 7, including, for comparison, the Sr–Nd isotope compositions of UHP eclogites from Yangkou (Chen, Ye, & Liu, 2002). Initial $^{87}Sr/^{86}Sr$ ratios and $\varepsilon_{Nd}(t)$ values (for definition of $\varepsilon_{Nd}(t)$ see Table S4) were corrected to the metamorphic age of t = 221 Ma for all samples based on the U–Pb zircon ages reported below. The granite has moderate initial $^{87}Sr/^{86}Sr$ ratios of 0.7078–0.7110 and negative $\varepsilon_{Nd}(t)$ values ranging from −21.9 to −15.6, yielding two-stage depleted mantle Nd model ages of 2,776–2,259 Ma. The eclogites exhibit moderate and consistent initial $^{87}Sr/^{86}Sr$ ratios of 0.7068–0.7088 and negative $\varepsilon_{Nd}(t)$ values of −16.5 to −11.6, yielding two-stage depleted mantle Nd model ages of 2,334–1,926 Ma, while the gneisses have variably high initial $^{87}Sr/^{86}Sr$ ratios of 0.7093–0.7168 and much more negative $\varepsilon_{Nd}(t)$ values of −22.2 to −18.1, corresponding to two-stage depleted mantle Nd model ages of 2,796–2,467 Ma.

4.4 | Zircon morphology

Zircon grains from both components of the composite veins show similar morphological features. They are generally colourless and transparent in plane light, euhedral to subhedral and equant to prismatic, with crystal lengths varying from 50 to 300 μm and aspect ratios (length/width) of 1:1 to 4:1. Most grains show a distinct core–mantle structure in cathodoluminescence (CL) images (Figure 8a,b). The cores show rhythmic oscillatory or sector zoning with weak to moderate luminescence, whereas the overgrowths, which have sharp contacts against the cores, are unzoned or weakly zoned with moderate luminescence. In some cases, the mantles are incompletely surrounded by a thin outer rim (<5 μm) that is CL-bright (Figure 8a,b). In addition,

there are zircon grains that are unzoned or weakly zoned and exhibit moderate luminescence in CL images (Figure 8a,b), similar to the mantle domains. These grains also may have thin CL-bright rims.

Zircon grains from the host eclogite are mostly yellowish or murky-brown to colourless in plane light, whereas those from the gneiss are mostly colourless. Zircon grains from both are subhedral to anhedral and ovoid (in the eclogite), equant or prismatic (in both), with lengths ranging from 50 to 300 μm and aspect ratios of 1:1 to 4:1. In CL images, most zircon grains from eclogite and gneiss display overgrowths in sharp contact with cores (Figure 8c, d). In the eclogite, the zircon cores are irregular with weak oscillatory, patchy or planar zoning and weak to moderate luminescence, whereas the overgrowth mantles are unzoned or weakly zoned with relatively homogeneous moderate luminescence. In addition, some zircon grains in the eclogite are unzoned and resemble the mantles in CL images (Figure 8c). In the gneiss, the zircon cores exhibit oscillatory or sector zoning, whereas the mantles are unzoned; they exhibit homogeneous weak to moderate luminescence. In addition, the mantles may have thin (<5 μm) CL-bright rims, similar to those on zircon from the composite vein.

The outermost CL-bright rims on zircon from the composite vein and the gneiss are similar to those commonly seen in HP–UHP metamorphic rocks elsewhere in the Sulu belt (e.g. Gao, Zheng, Xia, & Chen, 2014; Xu et al., 2013). They may represent recrystallization of the outermost part of the mantle or new zircon growth (Corfu, Hanchar, Hoskin, & Kinny, 2003). However, they are too thin to be analysed by LA-ICP-MS or SIMS, and consequently are not discussed further.

4.5 | Zircon U–Pb ages and trace element compositions

4.5.1 | Eclogite

Zircon from two host eclogites (YK1412-13 and YK156-3; Tables S5a and S6a) was analysed for U–Pb isotope and trace element compositions. Zircon cores from YK1412-13 (n = 18) are characterized by high Th/U ratios (0.27–2.19, Figure S3a,b) and record $^{206}Pb/^{238}U$ dates varying from 778 ± 9 to 398 ± 7 Ma (Figure 9a). By contrast, overgrowth mantles and new grains (n = 19) have low Th/U ratios (0.004–0.030, Figure S3a,b); a subset of nine analyses with >90% concordance yields $^{206}Pb/^{238}U$ dates of 223 ± 7 to 214 ± 9 Ma and gives a weighted mean age of 217 ± 2 Ma (2σ, MSWD = 0.75, Figure 9a). Similarly, zircon cores from YK156-3 (n = 13) have high Th/U ratios (0.08–1. 91, Figure S3a,b) and yield $^{206}Pb/^{238}U$ dates ranging from 776 ± 9 to 462 ± 13 Ma (Figure 9b). By contrast, overgrowth mantles and new grains (n = 16) have low Th/U ratios (0.004–0.021, Figure S3a,b); a subset of eight analyses with >90% concordance yields $^{206}Pb/^{238}U$ dates of 222 ± 5 to 215 ± 5 Ma and gives a weighted mean age of 217 ± 2 Ma (2σ, MSWD = 1.3, Figure 9b).

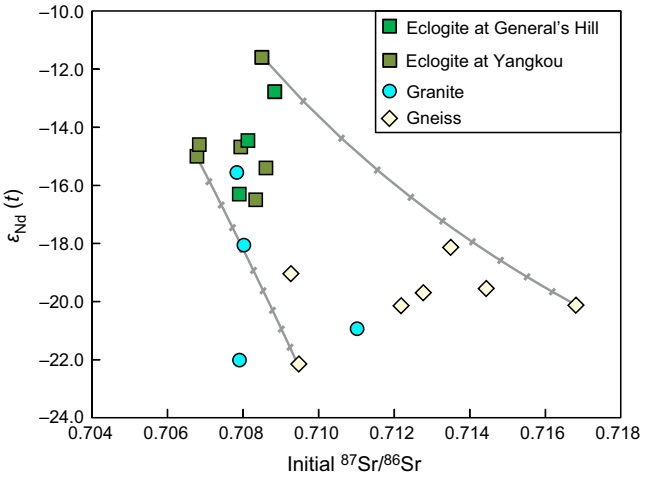

FIGURE 7 εNd(t) *v.* initial $^{87}Sr/^{86}Sr$ plot at t = 221 Ma for granite in the composite veins, the host eclogites and the surrounding gneisses. Whole-rock Sr–Nd isotope compositions of UHP eclogite at Yangkou, ~2 km to the north of General's Hill, are shown for comparison (from Chen et al., 2002). The two gray lines show results of modelling simple binary Sr–Nd isotope mixing of exemplar end-members of the eclogite and gneiss. Tick marks along mixing curve are at 10% increments

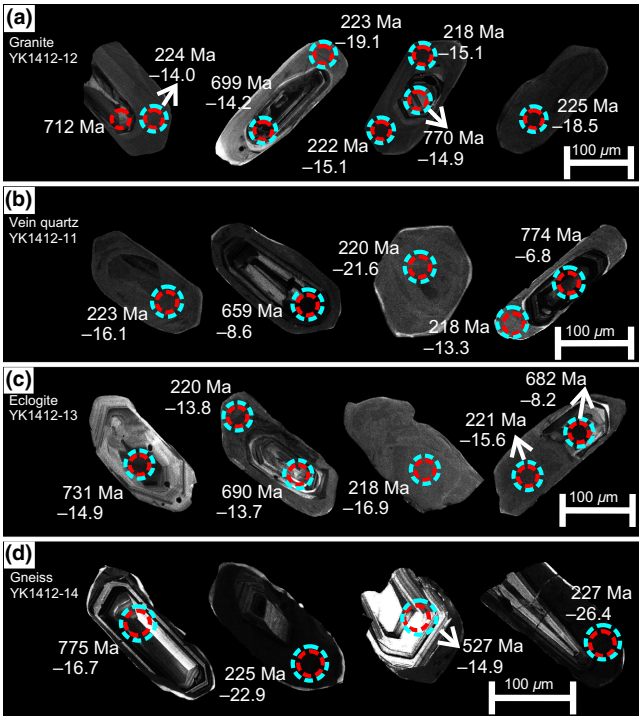

FIGURE 8 Cathodoluminescence images of representative zircon grains from one composite vein (a, granite; b, vein quartz), the host eclogite (c) and the surrounding gneiss (d). Circles mark the locations of LA(MC)-ICP-MS U–Pb (red) and Hf (light blue) isotope analyses

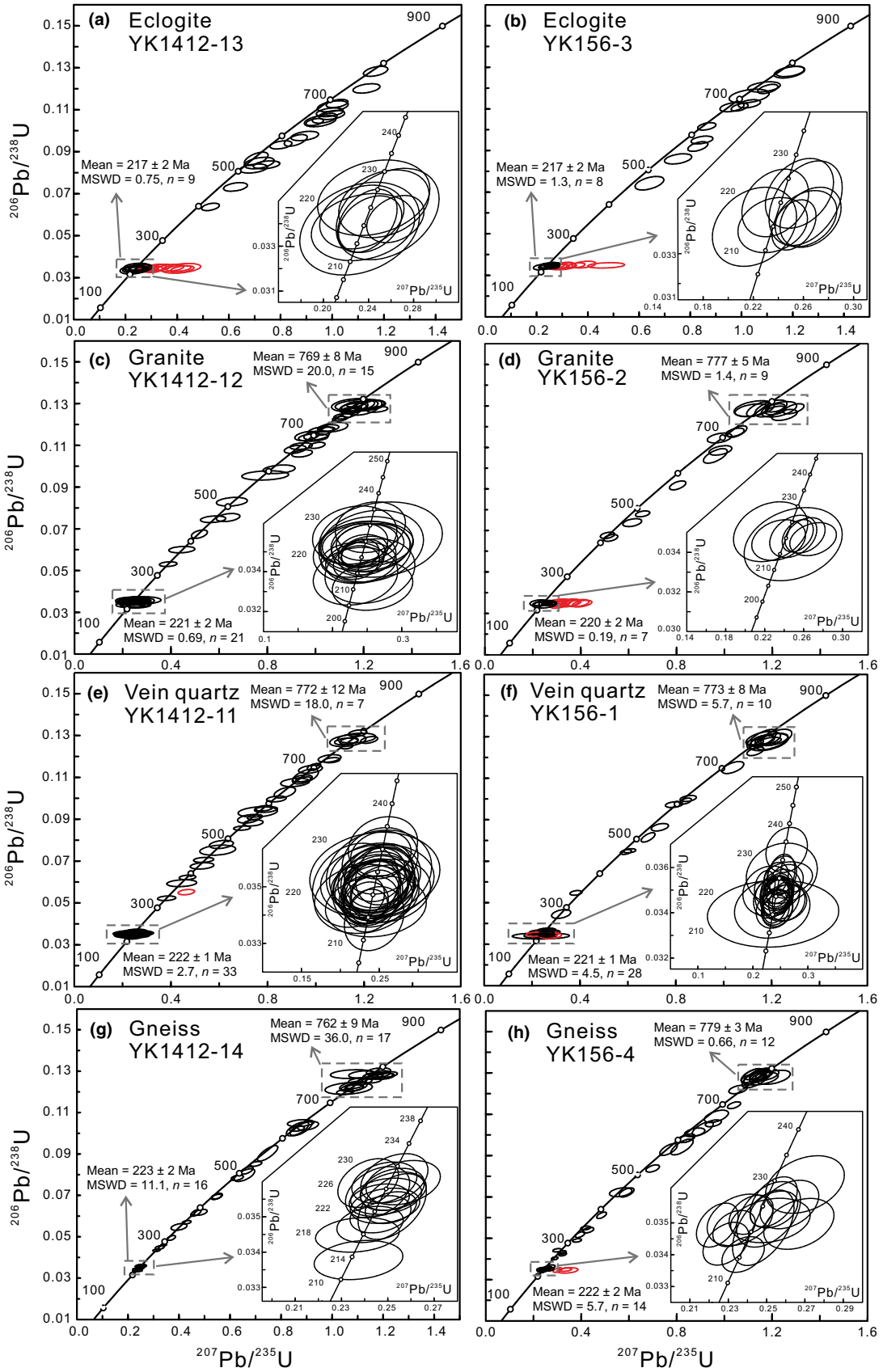

FIGURE 9 U–Pb concordia diagrams for zircon from the host eclogites (a, b), the granite (c, d) and vein quartz (e, f) from the composite veins, and the surrounding gneisses (g, h); the red circles represent analytical spots with <90% concordance. The insets are U–Pb concordia diagrams for concordant new zircon domains; the mean $^{206}Pb/^{238}U$ ages are given with 2σ uncertainty

Trace element compositions of zircon are illustrated in Figure 10a,b. The cores with variably low Hf/Y ratios (1.0–100.2) have high total REE abundances (∑REE = 343–13,702 ppm) and elevated chondrite-normalized HREE patterns [$(Gd/Lu)_N$ = 0.012–0.520], with positive Ce (Ce/Ce* = 2.3–641.9) and negative Eu (Eu/Eu* = 0.23–0.81) anomalies. By contrast, the overgrowth mantles and new grains have higher Hf/Y ratios (110.9–478.0) but lower total REE abundances (∑REE = 38–161 ppm) and flatter chondrite-normalized HREE patterns [$(Gd/Lu)_N$ = 0.579–2.898]; most have negligible to weakly positive Eu anomalies (Figure S4, Eu/Eu* = 0.67–2.02).

4.5.2 | Granite

U–Pb isotope and trace element compositions were determined for zircon from two samples of granite from the composite veins (YK1412-12 and YK156-2; Tables S5b and S6b). Zircon cores from YK1412-12 (n = 34) are characterized by high Th/U ratios (0.17–1.62, Figure S3c,d). They yield $^{206}Pb/^{238}U$ dates varying from 786 ± 5 to 333 ± 5 Ma, while a subset of 15 analyses with >90% concordance yields $^{206}Pb/^{238}U$ dates of 784 ± 12 to 747 ± 4 Ma and gives a weighted mean age of 769 ± 8 Ma (2σ, MSWD = 20.0, Figure 9c). Similarly, cores from YK156-2 (n = 19) have high Th/U ratios (0.18–2.78, Figure S3c,d) and yield $^{206}Pb/^{238}U$ dates ranging from 782 ± 8 to 414 ± 7 Ma. Nine analyses with >90% concordance yield $^{206}Pb/^{238}U$ dates from 782 ± 8 to 763 ± 10 Ma that give a weighted mean age of 777 ± 5 Ma (2σ, MSWD = 1.4, Figure 9d).

Overgrowth mantles and new grains of zircon from YK1412-12 (n = 21) and YK156-2 (n = 18) have low Th/U ratios of 0.003–0.027 and 0.004–0.014, respectively (Figure S3c,d). New zircon with >90% concordance yields $^{206}Pb/^{238}U$ dates of 229 ± 5 to 211 ± 5 Ma and 222 ± 6 to 218 ± 8 Ma, respectively. These dates give consistent weighted mean ages of 221 ± 2 Ma (2σ, MSWD = 0.69, Figure 9c; n = 21) and 220 ± 2 Ma (2σ, MSWD = 0.19, Figure 9d; n = 7).

Zircon from the two samples has similar trace element compositions for the cores, overgrowth mantles and new grains (Table S6b). The cores contain high total REE abundances (∑REE = 134–9,231 ppm) and show variably low Hf/Y ratios of 1.3–66.5. In chondrite-normalized REE diagrams (Figure 10c,d), they are characterized by steep HREE patterns [$(Gd/Lu)_N$ = 0.076–0.858], and pronounced positive Ce (Ce/Ce* = 6.0–438.1) and negative Eu (Eu/Eu* = 0.08–0.41) anomalies. By contrast, the overgrowth mantles and new grains have lower total REE abundances (∑REE = 21–288 ppm) than the cores, with higher Hf/Y ratios of 76.32–479.27. They exhibit flatter chondrite-normalized HREE patterns [$(Gd/Lu)_N$ = 0.031–1.958], with similar positive Ce (Ce/Ce* = 0.7–152.1), but mostly weakly negative Eu anomalies (Figure S4, Eu/Eu* = 0.09–1.67; Figure 10c,d).

4.5.3 | Vein quartz

U–Pb isotope and trace element compositions were determined for zircon from two samples of the vein quartz (YK1412-11 and YK156-1; Tables S5c and S6c). Cores from YK1412-11 (n = 32) have high Th/U ratios (0.05–1.81, Figure S3e,f) and give $^{206}Pb/^{238}U$ dates varying from 794 ± 6 to 328 ± 4 Ma, with a subset of seven analyses with >90% concordance yielding $^{206}Pb/^{238}U$ dates of 794 ± 6 to 758 ± 4 Ma and a weighted mean age of 772 ± 12 Ma (2σ, MSWD = 18.0, Figure 9e). Similarly, cores from YK156-1 (n = 20) have high Th/U ratios (0.24–1.78, Figure S3e,f) and give $^{206}Pb/^{238}U$ dates ranging from 782 ± 14 to 281 ± 9 Ma; the 10 least recrystallized spots have concordant $^{206}Pb/^{238}U$ dates of 782 ± 14 to 748 ± 8 Ma that yield a weighted mean age of 773 ± 8 Ma (2σ, MSWD = 5.7, Figure 9f).

Overgrowth mantles and new grains of zircon from the two samples (n = 33 and 31, respectively) have low Th/U ratios of 0.003–0.029 and 0.005–0.060 (Figure S3e,f). New zircon domains with >90% concordance record $^{206}Pb/^{238}U$ dates of 231 ± 4 to 215 ± 5 Ma and 233 ± 4 to 215 ± 6 Ma, respectively, and yield weighted mean ages of 222 ± 1 Ma (2σ, MSWD = 2.7, Figure 9e; n = 33) and 221 ± 1 Ma (2σ, MSWD = 4.5, Figure 9f; n = 28).

Zircon cores with low Hf/Y ratios (2.6–185.0) are characterized by high total REE contents (∑REE = 55–7,199 ppm) and steep chondrite-normalized HREE patterns [$(Gd/Lu)_N$ = 0.109–0.402], with positive Ce (Ce/Ce* = 10.3–184.1) and negative Eu (Eu/Eu* = 0.04–0.80) anomalies (Figure 10e,f). By contrast, the overgrowth mantles and new grains have high Hf/Y ratios of 69.9–400.9. They are depleted in REE abundances (∑REE = 21–215 ppm) and exhibit flatter chondrite-normalized HREE patterns [$(Gd/Lu)_N$ = 0.056–3.609] than the cores, mostly with positive Ce (Ce/Ce* = 0.3–101.7) and weakly negative to moderately positive Eu anomalies (Figure S4, Eu/Eu* = 0.27–4.30).

4.5.4 | Gneiss

Zircon from two gneiss samples was analyzed for U–Pb isotope and trace element compositions (YK1412-14 and YK156-4; Tables S5d and S6d). Zircon cores from YK1412-14 (n = 37) show high Th/U ratios (0.06–1.96, Figure S3g, h) and record $^{206}Pb/^{238}U$ dates ranging from 787 ± 7 to 274 ± 2 Ma; 17 analyses with >90% concordance yield $^{206}Pb/^{238}U$ dates from 787 ± 7 to 731 ± 5 Ma that give a weighted mean age of 762 ± 9 Ma (2σ, MSWD = 36.0, Figure 9g). Similarly, cores from YK156-4 (n = 34) give

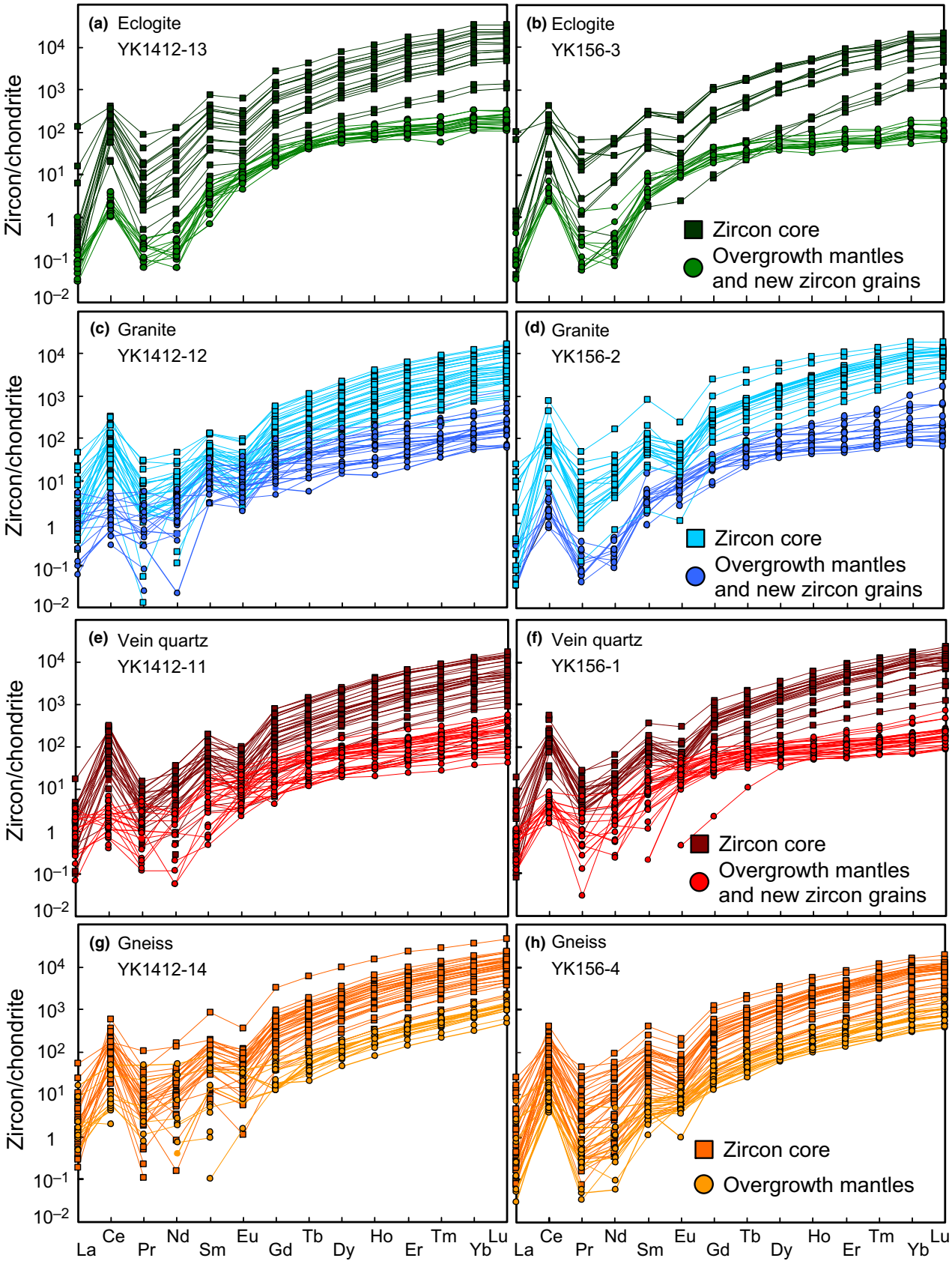

FIGURE 10 Chondrite-normalized rare earth element patterns of zircons from the host eclogites (a, b), the granite (c, d) and vein quartz (e, f) from the composite veins, and the surrounding gneisses (g, h). Normalization values are from Sun and McDonough (1989)

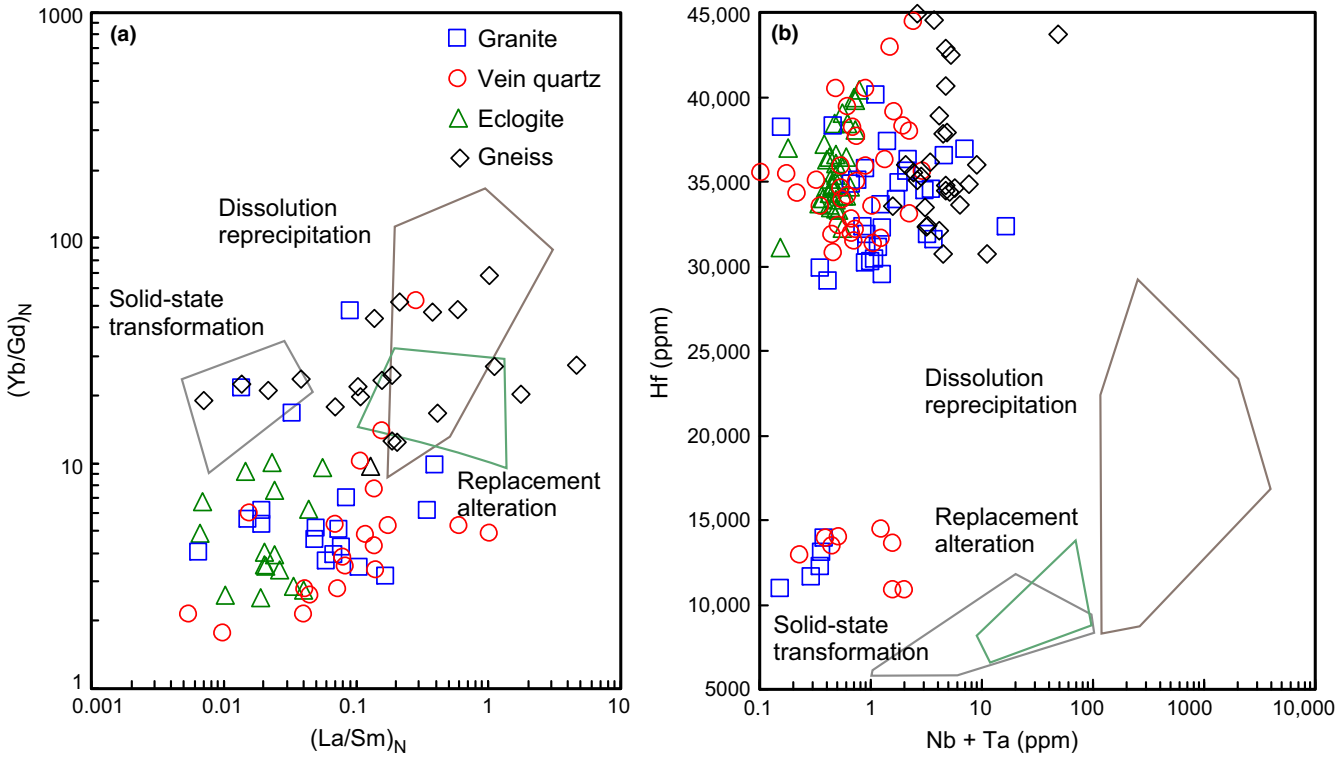

FIGURE 11 Trace element composition of zircon overgrowth mantles and new zircon grains from the composite granite–quartz veins, their host eclogites and the surrounding gneisses plotted on the (Yb/Gd)N *v*. (La/Sm)N (a) and Hf (ppm) *v*. Nb+Ta (ppm) (b) discrimination diagrams of Xia et al. (2010) as modified by Zheng and Hermann (2014)

$^{206}Pb/^{238}U$ dates varying from 784 ± 10 to 267 ± 3 Ma; the 12 least recrystallized zircon grains with >90% concordance record $^{206}Pb/^{238}U$ dates from 784 ± 10 to 776 ± 13 Ma that give a weighted mean age of 779 ± 3 Ma (2σ, MSWD = 0.66, Figure 9h). By contrast, overgrowth mantles (n = 16 and 17, respectively) from zircon in the gneisses are characterized by low Th/U ratios (0.007–0.026 and 0.008–0.075, Figure S3g,h). Analyses with >90% concordance yield $^{206}Pb/^{238}U$ dates of 228 ± 3 to 213 ± 2 Ma and 229 ± 4 to 216 ± 2 Ma, respectively that give weighted mean ages of 223 ± 2 (2σ, MSWD = 11.1, Figure 9g; n = 16) and 222 ± 2 Ma (2σ, MSWD = 5.7, Figure 9h; n = 14).

Trace element compositions of zircon are shown in Figure 10g,h. The cores have variably low Hf/Y ratios (1.2–95.4) and high total REE concentrations (∑REE = 229–16,263 ppm). They show steep chondrite-normalized HREE patterns [$(Gd/Lu)_N$ = 0.086–0.499], and strongly positive Ce (Ce/Ce* = 2.3–347.3) and negative Eu (Eu/Eu* = 0.07–0.67) anomalies. Compared to the cores, the overgrowth mantles have higher Hf/Y ratios (43.7–253.4) and lower total REE abundances (∑REE = 114–492 ppm; Table S6d), but exhibit similar sloping chondrite-normalized HREE patterns [$(Gd/Lu)_N$ = 0.066–0.451] mostly with weakly to moderately negative Eu anomalies (Figure S4, Eu/Eu* = 0.1–1.32).

4.5.5 | Trace element discrimination diagrams for new zircon

In Figure 11 we show the trace element composition of zircon overgrowths and new zircon grains from the composite granite–quartz veins, their host eclogites and the surrounding gneisses plotted on the discrimination diagrams of Xia et al. (2010) as modified by Zheng and Hermann (2014). Most of the new zircon in the rocks at General's Hill is characterized by low $(Yb/Gd)_N$ (Figure 11a) and high Hf at low Nb+Ta (Figure 11b); a small proportion of new zircon from the composite veins plots at low Hf as well as low Nb+Ta (Figure 11b). Although some of the new zircon in the $(Yb/Gd)_N$ *v*. $(La/Sm)_N$ plot (Figure 11a) overlaps the fields defined by Xia et al. (2010) for dissolution–reprecipitation, replacement alteration and solid-state recrystallization, there is no overlap in the Hf *v*. Nb+Ta plot (Figure 11b).

4.6 | Zircon Hf–O isotope compositions

4.6.1 | Eclogite

For zircon from one of the eclogite samples (YK1412-13), the cores (n = 13) record high $^{176}Lu/^{177}Hf$ ratios of 0.000347–0.003385 but low $^{176}Hf/^{177}Hf$ ratios of 0.281853–0.282169 (Table S7; Figure S5a,b). At

t_1 = 780 Ma, the calculated $\varepsilon_{Hf}(t_1)$ values (for definition and calculation of $\varepsilon_{Hf}(t)$ see Appendix S1 and Table S7) are −16.1 to −4.3 with a weighted mean of −12.4 ± 2.1 (MSWD = 22; Figure 12a), yielding T_{DM1} (for definition and calculation of T_{DM} see Appendix S1 and Table S7) ages varying from 1,980 ± 29 to 1,500 ± 39 Ma. On the other hand, the overgrowth mantles and new grains (n = 19) exhibit low $^{176}Lu/^{177}Hf$ ratios of 0.000006–0.001883 but high $^{176}Hf/^{177}Hf$ ratios of 0.282124–0.282265 (Table S7; Figure S5a,b), which yield initial $^{176}Hf/^{177}Hf$ ratios of 0.282116 to 0.282265 and $\varepsilon_{Hf}(t_2)$ values of −18.4 to −13.1 at 221 Ma (Figures 12a and 13). The zircon cores (n = 24) record $\delta^{18}O$ values from 5.61 to 6.82‰, whereas the overgrowth mantles and new grains (n = 36) show slightly lower $\delta^{18}O$ values of 5.33–5.93‰ (Table S8; Figure 14a,b).

4.6.2 | Composite vein

For zircon from one of the granite samples (YK1412-12), the cores (n = 21) have relatively high $^{176}Lu/^{177}Hf$ ratios of 0.000355–0.001778 and low $^{176}Hf/^{177}Hf$ ratios of 0.281845–0.282054 (Table S7; Figure S5c,d). Assuming t_1 = 780 Ma, the calculated $\varepsilon_{Hf}(t_1)$ values are −16.5 to −8.5 (Figure 12b), yielding T_{DM2} of 2,706 ± 102 to 2,209 ± 63 Ma. By contrast, the overgrowth mantles and new zircon grains (n = 18) have lower $^{176}Lu/^{177}Hf$ ratios of 0.000014–0.000903 but higher $^{176}Hf/^{177}Hf$ ratios of 0.282015–0.282245 compared to those of the cores (Table S7; Figure S5c,d). At t_2 = 221 Ma, the calculated initial $^{176}Hf/^{177}Hf$ ratios and $\varepsilon_{Hf}(t_2)$ values are 0.282013 to 0.282244 and −22.0 to −14.4, respectively (Figures 12b and 13). The overgrowth mantles and new grains of zircon (n = 51) have $\delta^{18}O$ values of 5.25–5.98‰, slightly lower than the cores (n = 25), which have homogeneous $\delta^{18}O$ values from 5.47 to 6.41‰ (Table S8; Figure 14c,d).

For zircon from one of the vein quartz samples (YK1412-11), the cores (n = 23) have high $^{176}Lu/^{177}Hf$ ratios of 0.000443–0.002185, but variably low $^{176}Hf/^{177}Hf$ ratios of 0.281861–0.282193 (Table S7; Figure S5e,f). At t_1 = 780 Ma, their $\varepsilon_{Hf}(t_1)$ values are −16.9 to −4.0 with a weighted mean of −9.5 ± 1.6 (MSWD = 16; Figure 12c), corresponding to T_{DM2} ages of 2,669 ± 76 to 1,930 ± 105 Ma. By contrast, overgrowth mantles and new grains (n = 18) have relatively low $^{176}Lu/^{177}Hf$ ratios of 0.000020–0.001000 and high $^{176}Hf/^{177}Hf$ ratios of 0.281991–0.282258 (Table S7; Figure S5e,f). At t_2 = 221 Ma, the calculated initial $^{176}Hf/^{177}Hf$ ratios are 0.281988 to 0.282258 (Figure 13), corresponding to $\varepsilon_{Hf}(t_2)$ values of −22.9 to −13.3 with a weighted mean of −18.2 ± 1.5 (MSWD = 10.2; Figure 12c). The zircon cores (n = 25) record $\delta^{18}O$ values of 5.46–6.67‰, whereas the overgrowth mantles and new grains (n = 44) have slightly lower $\delta^{18}O$ values of 5.19–6.06‰ (Table S8; Figure 14e,f).

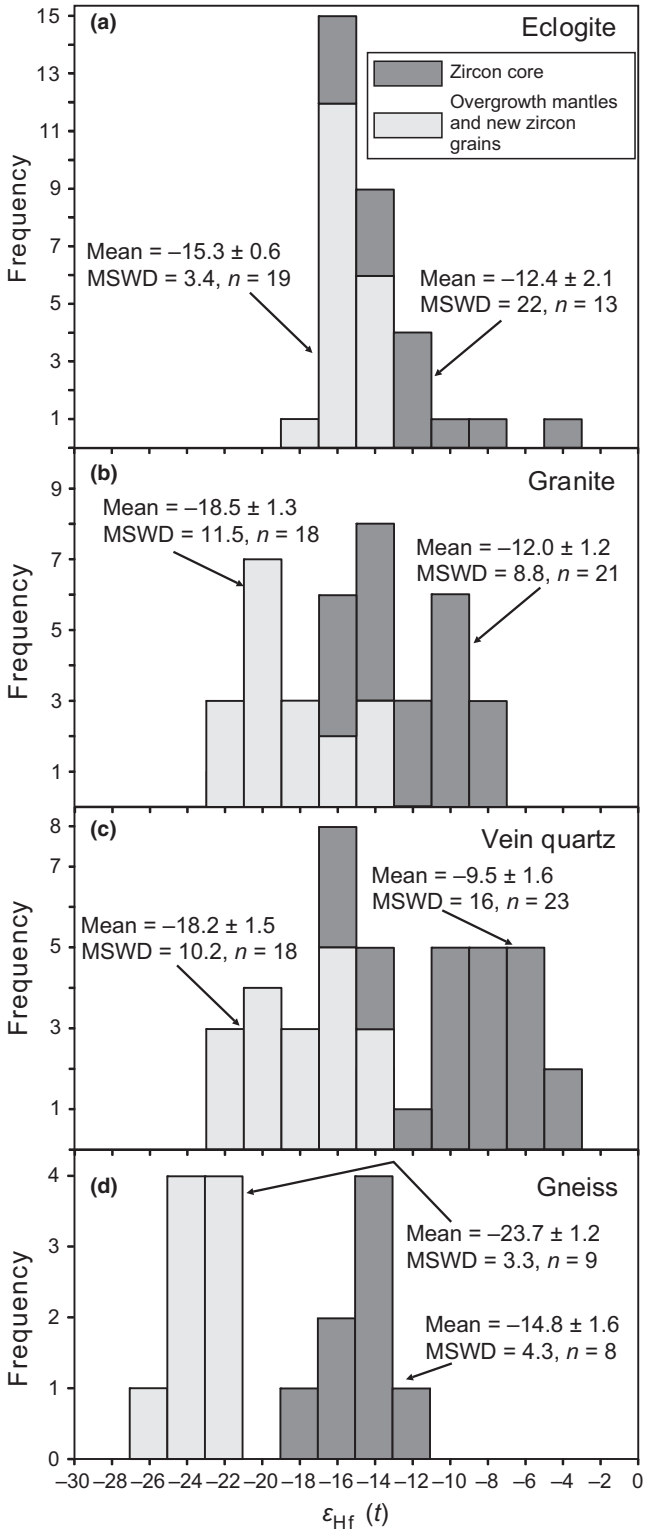

FIGURE 12 Histogram of εHf(t) values at t_1 = 780 Ma for zircon cores and at t_2 = 221 Ma for new zircon grains and/or overgrowth mantles from the host eclogite (a), the granite (b) and vein quartz (c) from one composite vein, and the surrounding gneiss (d)

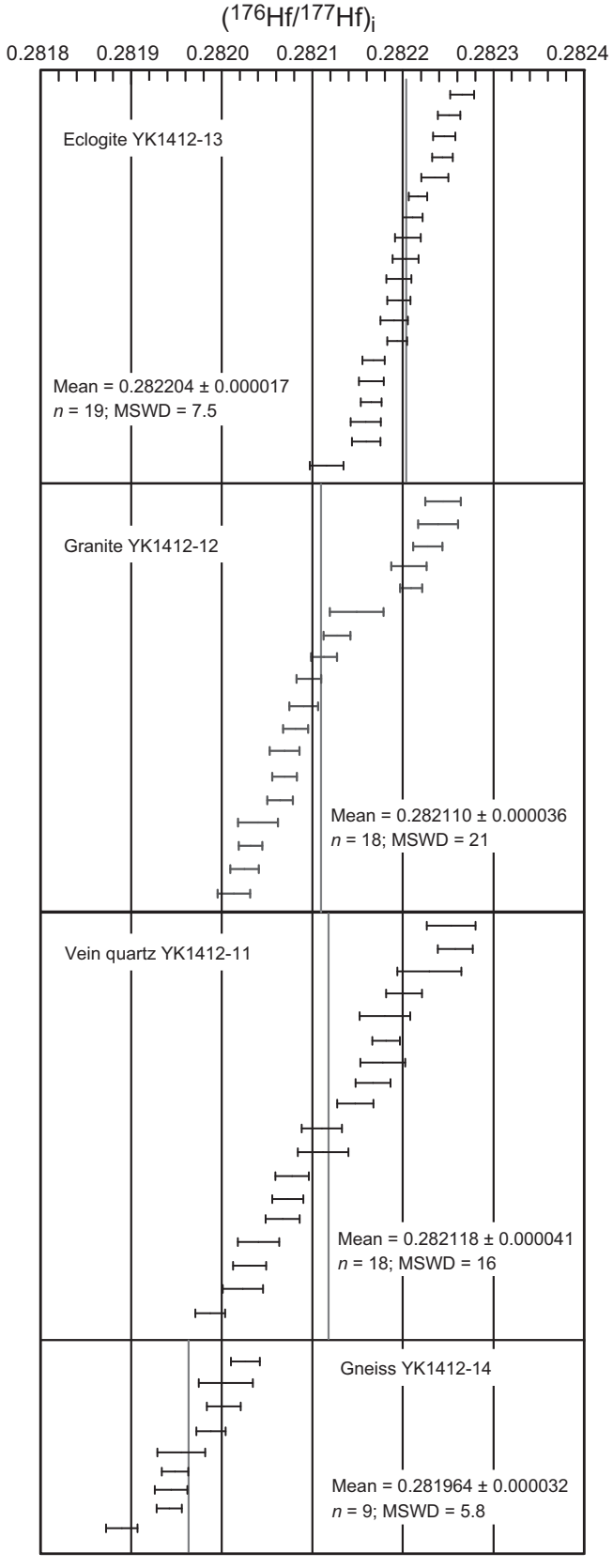

FIGURE 13 Comparison of initial $^{176}Hf/^{177}Hf$ ratios [$(^{176}Hf/^{177}Hf)_i$] at t_2 = 221 Ma for new zircon grains and/or overgrowth mantles from the host eclogite, the granite and vein quartz from one composite vein, and the surrounding gneiss

4.6.3 | Gneiss

For zircon from one of the gneiss samples (YK1412-14), the cores (n = 8) have $^{176}Lu/^{177}Hf$ ratios of 0.000992–0.002155 and $^{176}Hf/^{177}Hf$ ratios of 0.281807–0.281951 (Table S7; Figure S5 g,h). The calculated $\varepsilon_{Hf}(t_1)$ values at 780 Ma are −18.0 to −12.4 with a weighted mean of −14.8 ± 1.6 (MSWD = 4.3; Figure 12d), yielding T_{DM2} ages from 2,801 ± 95 to 2,451 ± 85 Ma. By contrast, the overgrowth mantles (n = 9) record lower $^{176}Lu/^{177}Hf$ ratios of 0.000115–0.001077 but variably high $^{176}Hf/^{177}Hf$ ratios of 0.281894–0.282027 when compared to the cores (Table S7; Figure S5g,h). At t_2 = 221 Ma, the calculated initial $^{176}Hf/^{177}Hf$ ratios and $\varepsilon_{Hf}(t_2)$ values are 0.281890–0.282026 and −26.4 to −21.5, respectively (Figures 12d & 13). The cores (n = 23) have $\delta^{18}O$ values of 5.82–6.67‰, slightly higher than those of the overgrowth mantles (n = 38) with $\delta^{18}O$ values of 5.30–6.29‰ (Table S8; Figure 14g,h).

4.7 | Ti-in-zircon thermometry

The solubility of Ti in zircon shows strong dependence on temperature. For zircon that grew in equilibrium with an appropriate mineral assemblage to buffer the activity of Ti (a_{TiO_2}; buffered by rutile, titanite or ilmenite) and silica (a_{SiO_2}; buffered by a SiO_2 phase), the Ti concentration has been calibrated as a thermometer (Ferry & Watson, 2007). Because zircon is extremely retentive of Ti, the Ti-in-zircon thermometer is robust in preserving temperatures of zircon growth (Cherniak & Watson, 2007).

The Ti-in-zircon thermometer of Ferry and Watson (2007) is used to constrain the crystallization temperature of overgrowth mantles and/or new grains of zircon in the host eclogite, the granite and vein quartz from the composite veins, and the surrounding gneiss. This thermometer was calibrated at 1.0 GPa and has a positive pressure dependence of ~50°C/GPa (Ferry & Watson, 2007, p. 711). To correct the calculated temperatures for pressure, the pressure of crystallization of the granite was calculated using the Si content of phengite (Caddick & Thompson, 2008, eq. 8). Calculated pressures in the granite from the composite veins (3.40–3.29 Si pfu) are summarized in a box-and-whisker plot in Figure S6a, for which the interquartile range is 2.5–2.1 GPa.

Overgrowth mantles and/or new grains of zircon from the eclogite, the granite and vein quartz, and the gneiss have Ti concentrations that vary from 3 to 38 ppm, 1 to 33 ppm, <1 to 65 ppm and <1 to 60 ppm, respectively (Table S6). As quartz is a major mineral in all samples, a_{TiO_2} is taken as 1. Rutile is the major Ti-rich mineral in the eclogite; in the granite from the composite veins, rutile

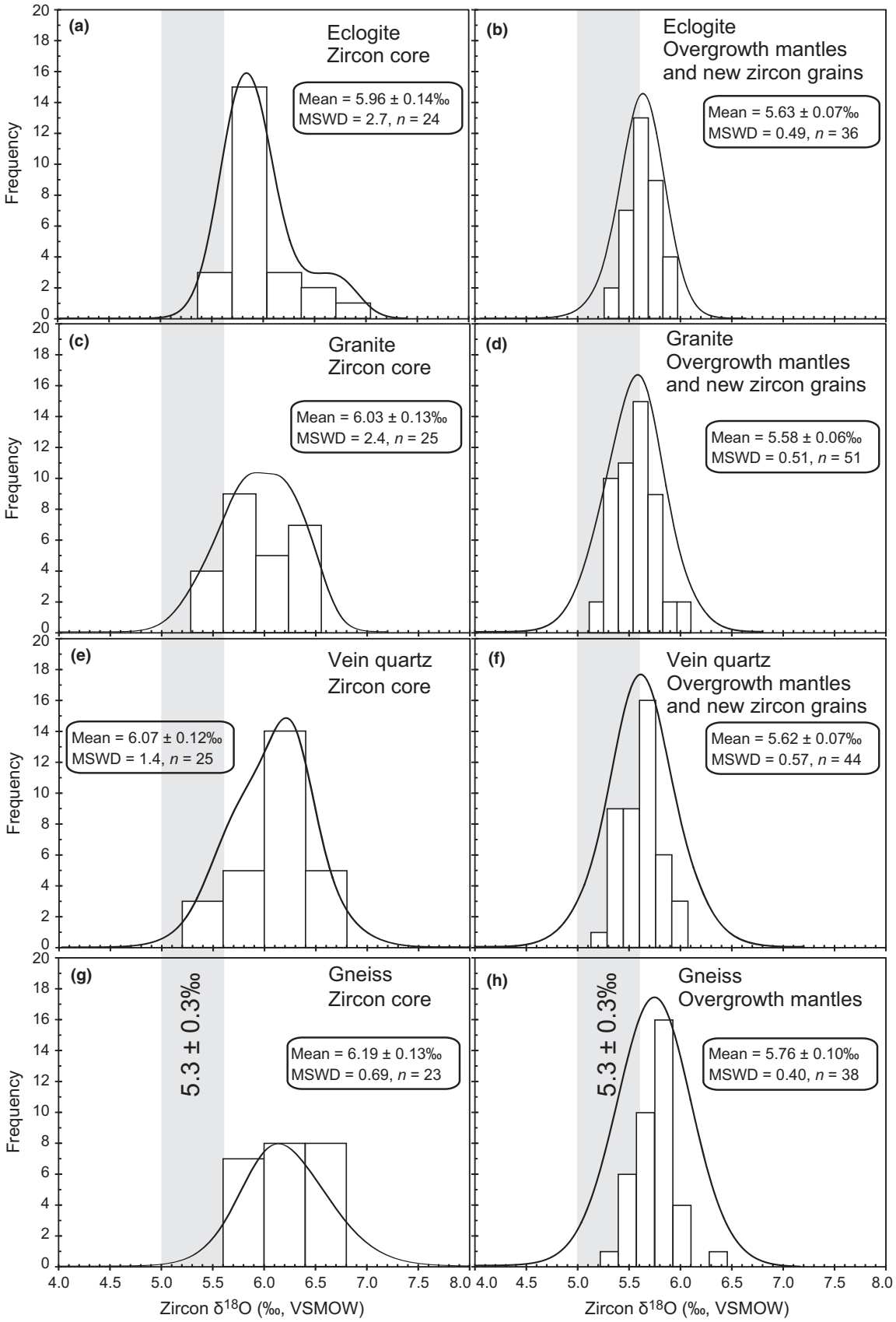

FIGURE 14 Histograms of $\delta^{18}O$ values for zircon from the host eclogite (a, b), the granite (c, d) and vein quartz (e, f) from one composite vein, and the surrounding gneiss (g, h). The $\delta^{18}O$ value of the mantle (5.3 ± 0.3‰) is from Valley et al. (1998). VSMOW, Vienna standard mean ocean water

occurs included in phengite, although titanite is the Ti-bearing mineral outside phengite. Therefore, we take a_{TiO2} in the eclogite and granite to be 1.0 (Watson, Wark, & Thomas, 2006). However, the a_{TiO_2} in the vein quartz is unconstrained, so temperatures calculated with a_{TiO_2} of 1.0 may be underestimates by up to 70°C at 750°C (Ferry & Watson, 2007). By contrast, titanite is the only Ti-rich mineral in the gneiss, which suggests that a_{TiO_2} was likely <1.0. Since the plausible lower limit of a_{TiO_2} in typical crustal rocks is 0.5 (Ferry & Watson, 2007; Hayden & Watson, 2007), this value is used in calculating temperatures from the gneiss.

The calculated Ti-in-zircon temperatures are corrected to 2.5 GPa and summarized in box-and-whisker plots in Figure S6b. For the granite, the interquartile range is 851–777°C, while the interquartile range for the vein quartz is 868–765°C. Similarly, for the host eclogite, the interquartile range is 839–784°C, consistent with that of 901–744°C for the gneiss. The median temperatures for all samples are ~820°C. These temperatures will be ~20°C lower at 2.1 GPa.

4.8 | Phase equilibria modelling

Figure 15 shows a *P*–*T* pseudosection calculated in the MnO–Na_2O–CaO–K_2O–FeO–MgO–Al_2O_3–SiO_2–H_2O–TiO_2–O (MnNCKFMASHTO) model system for the composition of a granite sample (YK1412-12) from one composite vein. Phase equilibria calculations use the major element oxide bulk composition as determined by wet chemical analysis, assuming all loss on ignition as H_2O and an $Fe^{3+}/\Sigma Fe$ ratio of 0.2. Calculations were undertaken using THERMOCALC (Powell & Holland, 1988) and the end-member thermodynamic data of Holland and Powell (2011; ds62 dataset as generated on 06/02/14). Activity–composition models used are those calibrated for pelitic systems (White, Powell, Holland, Johnson, & Green, 2014; White, Powell, & Johnson, 2014). For clinopyroxene the supra-solidus "augite" model of Green, White, Diener, Powell, and Holland (2016) is used. Although this was calibrated against a different ("mafic") thermodynamic model for melt, it is the only available high-*T* (i.e. containing tetrahedral Al) clinopyroxene model. Similarly, the high-*T* hornblende model is from Green et al. (2016). The original thermodynamic model for haplogranite melt was formally calibrated up to only 1.0 GPa (Holland & Powell, 2001). Extrapolation of the thermodynamic model for melt to very high pressures may introduce errors, so we have limited the pressure range of the *P*–*T* pseudosection to <1.5 GPa, which is lower than the fluid-absent solidus for phengite breakdown. Phase abbreviations in Figure 15 follow Whitney and Evans (2010).

The fields appropriate to the development of the microstructures interpreted to record phengite breakdown melting and melt crystallization (Figure 4e–i), and replacement of garnet by hornblende+plagioclase+opaque oxide

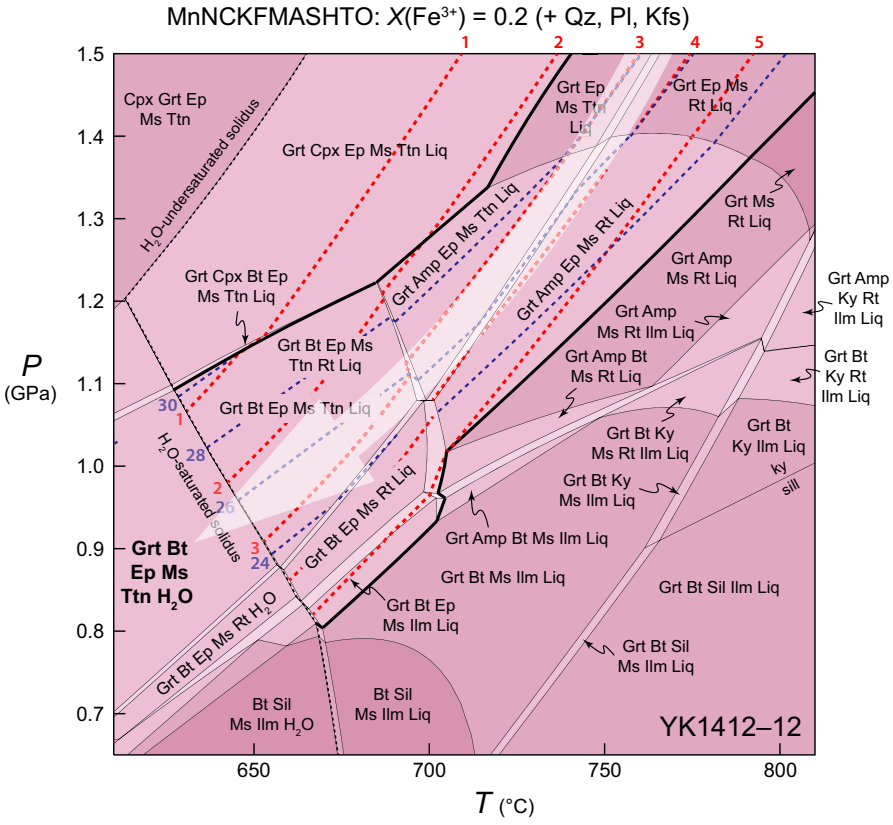

FIGURE 15 Phase equilibria modelling results in the MnNCKFMASHTO model system based on the composition of the granite vein sample YK1412-12. The bulk composition assumes an H_2O content equivalent to the loss on ignition and $Fe^{3+}/\Sigma Fe$ of 0.2. The fields appropriate to development of the microstructures interpreted to record decompression melting of phengite (Figure 4e–i) are enclosed within the bold lines and bounded by the H_2O-saturated solidus. These fields are contoured for the calculated abundance (mol.%) of melt (red dashes) and phengitic white mica (Ms; blue dashes). The white arrow shows a segment of the retrograde *P*–*T* path consistent with petrographic observations

(Figure 4c) during decompression are indicated by the heavy black lines. These fields all contain garnet, epidote, phengitic white mica (Ms) and melt, and are bound to lower temperature by the H_2O-saturated solidus (Figure 15). In Figure 15, at higher-*P*/lower-*T*, clinopyroxene (omphacite) is predicted to be stable, whereas at higher-*T*/lower-*P*, epidote is not predicted to be stable, and rutile does not occur at lower-*T*.

The observed petrographic features constrain the retrograde *P–T* evolution of the granite to this central swath in which both pressure and temperature decline, similar to the *P–T* path shown by the white arrow (Figure 15). The evidence of rutile included in phengite, titanite outside phengite and phengite breakdown, combined with the phase equilibria shown in Figure 15, including the calculated isopleths for melt and phengite, suggests limited melt production by reactions consuming phengite. Phengite breakdown began at >1.5 GPa, outside of the range of the calculations, and may have continued during cooling along the upper pressure part of the white arrow, as suggested by crossing the mol.% melt isopleths. However, along the exemplar *P–T* path the modelled amount of melt is small, being ~3–4 mol.% from 1.5 to 1.1 GPa, before decreasing to the solidus; the predicted amount of phengite decreases by a few mol.% from 1.5 GPa to the solidus. The final subsolidus phase assemblage of Grt+Bt+Ep+Ms+Ttn+H_2O (+Qz+Pl+Kfs) is shown in bold in Figure 15. Thus, the best estimate for final equilibration of the granite in the composite veins, assuming H_2O saturation was attained, is 0.7–1.1 GPa at <670°C (Figure 15).

5 | DISCUSSION

5.1 | Age and nature of the protoliths at General's Hill

The zircon cores in the eclogite show weak oscillatory, patchy or planar zoning, variable but high Th/U and low Hf/Y ratios, and steep HREE patterns with negative Eu anomalies. These features all point to a magmatic origin, indicating that the cores were inherited from the protolith of the eclogite (Guo, Wang, Liu, & Zi, 2016; Hoskin & Ireland, 2000; Wu & Zheng, 2004; Xiong, Ma, Jiang, & Zhang, 2016). The cores yield $^{206}Pb/^{238}U$ dates from *c.* 780 to *c.* 400 Ma, suggesting various degrees of solid-state recrystallization (e.g. Xia, Zheng, Yuan, & Wu, 2009; Zheng et al., 2004). The oldest $^{206}Pb/^{238}U$ dates of 778 ± 9 Ma and 776 ± 9 Ma, respectively, from the two samples are concordant and are consistent with the extensively reported protolith ages of *c.* 780–750 Ma for UHP metamorphic rocks in the Sulu belt (e.g. Zheng, Chen, & Zhao, 2009; Zheng et al., 2005, 2006). Based on these results, we interpret the crystallization age of the protolith of the eclogite to be *c.* 780 Ma.

Solid-state recrystallization of zircon should not disturb the original magmatic Lu–Hf isotope signature (Chen, Zheng, & Xie, 2010; Xia et al., 2009; Zheng et al., 2005), so we may use the initial Hf isotope systematics of the zircon cores to characterize the protolith. The eclogites are basaltic in composition and the zircon cores have negative $\varepsilon_{Hf}(t_1)$ values of −16.1 to −4.3, corresponding to T_{DM1} ages of 1,980–1,500 Ma. The enriched signature suggests that ancient lithospheric mantle was involved in the source of the magmas (Chen, Zheng, Li, & Chen, 2014; Zheng et al., 2006, 2009). This interpretation is reinforced by the O isotope composition of the zircon cores, which yield $\delta^{18}O$ values of 5.61–6.82‰ that are higher than the normal mantle zircon value of 5.3 ± 0.3‰ (Valley, Kinny, Schulze, & Spicuzza, 1998; Valley et al., 2005). Thus, we conclude that the protolith magmas were derived from enriched mantle, possibly as old as Palaeoproterozoic.

The zircon cores in the gneiss exhibit similar features to those of the eclogites and also indicate a magmatic origin. The cores yield variable $^{206}Pb/^{238}U$ dates from *c.* 780 to *c.* 255 Ma, suggesting various degrees of Pb loss, whereas the least recrystallized zircon in the two gneisses gives weighted mean ages of 762 ± 9 Ma and 779 ± 6 Ma, respectively. Thus, the crystallization age of the protolith of the gneiss is similar to the eclogite.

The gneisses are granitic in composition, enriched in LREE with flat HREE patterns, and depleted in Nb, Ta, Sr but enriched in Th, U and Pb. These features resemble those of rocks from more extensive outcrops of granitic gneiss elsewhere in the Sulu belt (Tang et al., 2008; Xu et al., 2013; Zong et al., 2010), suggesting the protolith of the gneiss at General's Hill was similar throughout the belt. Furthermore, the $\delta^{18}O$ values of 5.82–6.67‰ from the zircon cores are inconsistent with a metasedimentary protolith [$\delta^{18}O$(WR) = 10–20‰; Eiler, 2001] or with granite derived from a metasedimentary source [$\delta^{18}O$(Zircon) >8‰, considering the fractionation of $\Delta^{18}O$(Zircon–WR) of ~−2‰ for granite; O'Neil & Chappell, 1977; Valley et al., 2005].

The zircon cores from the gneiss have a limited range of $\varepsilon_{Hf}(t_1)$ values of −18.0 to −12.4 at 780 Ma, corresponding to T_{DM2} ages of 2,801–2,451 Ma (six of eight are >2,500 Ma). This indicates that the protolith originated from a predominantly Neoarchean crustal source. Thus, the protoliths of the eclogites and gneisses were probably generated contemporaneously during an episode of bimodal magmatism along the periphery of the Yangtze Craton at *c.* 780 Ma, most likely as a response to the breakup of the supercontinent Rodinia (e.g. Li et al., 2003; Zheng et al., 2004, 2006).

In the composite veins, zircon cores from both granite and vein quartz exhibit well-developed zoning, have $^{206}Pb/^{238}U$ dates varying from *c.* 790 to *c.* 330 Ma and *c.* 790 to *c.* 280 Ma, respectively, with corresponding $\varepsilon_{Hf}(t_1)$

values ranging from −16.5 to −8.5 and −16.9 to −4.0, and $\delta^{18}O$ values of 5.47–6.51‰ and 5.46–6.67‰. These features resemble those of the inherited zircon cores from the host eclogite and the surrounding gneiss. Similar inherited magmatic zircon cores are commonly recognized in HP–UHP veins from elsewhere in the Dabie–Sulu orogen (e.g. Chen, Zheng, & Hu, 2012; Sheng, Zheng, Chen, Li, & Dai, 2012; Zong et al., 2010), where they have been interpreted as xenocrysts transported by melt and/or aqueous fluid. We interpret the zircon cores in the composite veins to have been derived in a similar manner.

5.2 | Fluid flow at General's Hill

5.2.1 | Timing of fluid flow

Resorption and new growth of zircon generally reflect the presence of fluids during metamorphism (Corfu et al., 2003; Li et al., 2004; Rubatto & Hermann, 2003; Wu et al., 2006). Thus, new zircon growth in the composite veins, the host eclogite and the surrounding gneiss likely records important information concerning the timing and source of fluids responsible for vein formation (Hoskin, 2005; Wu et al., 2009; Zheng & Hermann, 2014).

Overgrowth mantles on inherited cores and new grains of zircon in both the granite and vein quartz in the composite veins are euhedral, exhibit moderate luminescence in CL images, sometimes with weak zoning, and have sharp boundaries against the cores. This zircon consistently has lower Th/U (mostly <0.1) and $^{176}Lu/^{177}Hf$ ratios but variably higher $^{176}Hf/^{177}Hf$ compared to the cores, implying that the new zircon grew in association with the attending fluid and was not simply recrystallized *in situ* (Chen et al., 2010; Xia et al., 2009; Zheng et al., 2005). The new zircon from both the granite and vein quartz has low HREE contents with high Hf/Y ratios, and shows shallowly sloping to relatively flat HREE patterns with weakly negative (granite) to moderately positive (vein quartz) Eu anomalies. These features suggest that the new zircon grew in the presence of garnet but not feldspar, consistent with crystallization under eclogite facies conditions (Rubatto, 2002; Rubatto & Hermann, 2003, 2007; Whitehouse & Platt, 2003). Moreover, when compared to the magmatic zircon cores, the consistently low $^{176}Lu/^{177}Hf$ but variably high $^{176}Hf/^{177}Hf$ ratios of all the new zircon also indicate co-precipitation with garnet (Zheng et al., 2005), consistent with the presence of garnet in the granite.

The new zircon from both granite and vein quartz yields weighted mean $^{206}Pb/^{238}U$ ages of 222–220 Ma, identical within uncertainty. Because this zircon crystallized from the fluids that precipitated the composite veins, the ages are interpreted as registering the timing of an episode of fluid flow at *c.* 221 Ma. The age is younger than the peak UHP coesite eclogite facies metamorphism in the Sulu belt, which occurred between *c.* 235 and *c.* 225 Ma, but is synchronous with the HP quartz eclogite facies recrystallization at *c.* 225 to *c.* 215 Ma (Liu, Jian, Kröner, & Xu, 2006; Liu & Liou, 2011; Zhao et al., 2006). Therefore, the fluid event recorded by these ages is inferred to have occurred during exhumation of the Sulu belt from coesite eclogite to quartz eclogite facies conditions.

The new zircon from the host eclogites and surrounding gneisses yields weighted mean $^{206}Pb/^{238}U$ ages of 223–217 Ma that are identical within uncertainty, and consistent with the age of *c.* 221 Ma obtained from the composite veins, implying that fluid was present in the eclogite and gneiss contemporaneously with that forming the veins. This zircon also has contrasting trace element and Lu–Hf isotope compositions compared to the magmatic cores, consistent with growth related to the Triassic event.

5.2.2 | The source of the fluid

Multiple studies have documented that robust isotope systems are credible in determining the source of fluids attending metamorphism, which is essential to constrain the length scale of fluid flow during subduction and exhumation, and the formation of HP–UHP vein systems (e.g. Liu et al., 2014; Philippot & Selverstone, 1991; Scambelluri & Philippot, 2001; Verlaguet et al., 2011; Zhao et al., 2016). The range of initial $^{176}Hf/^{177}Hf$ ratios and the mean $\varepsilon Hf(t_2)$ values of the new zircon (Figures 12 and 13) in both components of the composite vein [$\varepsilon Hf(t_2)$ of -18.5 ± 1.3 (granite) and -18.2 ± 1.5 (vein quartz)] are consistent at $t_2 = 221$ Ma, and lie between the mean values recorded by new zircon in the host eclogite ($\varepsilon Hf(t_2)$ of -15.3 ± 0.6) and the surrounding gneiss ($\varepsilon Hf(t_2)$ of -23.7 ± 1.2). This observation suggests that zircon in the composite veins crystallized from a fluid intermediate in composition between the fluid expected to have been in equilibrium with eclogite and that in equilibrium with gneiss. From this inference we conclude that the composite veins were precipitated from a blended fluid derived by mixing of fluids derived from the eclogite and gneiss, rather than from an exotic fluid, which implies that fluid flow was restricted within the exhumed continental crust.

In addition, the $\varepsilon Hf(t_2)$ values of the new zircon from the composite veins show an approximately negative linear relationship with the corresponding $^{176}Lu/^{177}Hf$ ratios (Figure S7), with the lowest $^{176}Lu/^{177}Hf$ and the highest $\varepsilon Hf(t_2)$ values similar to those of the host eclogite, and the highest $^{176}Lu/^{177}Hf$ and the lowest $\varepsilon Hf(t_2)$ values approaching those of the surrounding gneiss. This relationship supports the interpretation that the zircon, and

by implication the composite veins, was precipitated from a hybrid fluid, with one end-member being in equilibrium with the eclogite with low $^{176}Lu/^{177}Hf$ ratios but high $\varepsilon Hf(t_2)$ values and the other end-member being in equilibrium with the gneiss with high $^{176}Lu/^{177}Hf$ but low $\varepsilon Hf(t_2)$ values.

The whole-rock Nd and zircon O isotope compositions are fully consistent with this conclusion. The granite in the composite veins shows variable $\varepsilon Nd(t)$ values between −15.6 and −21.9 at 221 Ma, spanning the range from those of the eclogite to those the gneiss (Figure 7). Further, new zircon from both components of the composite veins yields consistent $\delta^{18}O$ values of 5.25–5.98‰ and 5.19–6.06‰, respectively, which are indistinguishable from those of the eclogite ($\delta^{18}O$ values of 5.33–5.93‰) and the gneiss ($\delta^{18}O$ values of 5.30–6.29‰; Figure 14).

The new zircon from all samples in this study consistently shows positive $\delta^{18}O$ values that are similar to or slightly lower than the corresponding core domains (Figure 14). However, these values do not match the large-scale O isotope depletion signature for igneous and metamorphic zircon from other UHP metamorphic rocks exposed in the Sulu belt (e.g. Chen, Zheng, Chen, et al., 2011; He, Zhang, & Zheng, 2016; Tang et al., 2008; Zheng, Fu, Gong, & Li, 2003; Zheng et al., 2004). This difference implies that the gabbroic protoliths of the UHP eclogites at General's Hill may have been emplaced deep enough in the crust to have escaped the high-*T* meteoric–hydrothermal alteration that affected other rocks in the belt during the Neoproterozoic. The absence of a depleted O isotope signature requires that the fluid be locally sourced as well as internally (rock) buffered.

The new zircon in this study is compared to metamorphic zircon from low-*T* UHP metagranite from southeastern Dabieshan (Xia et al., 2010) in Figure 11. The new zircon from the composite granite–quartz veins, their host eclogite and the surrounding gneisses is clearly distinct from metamorphic zircon formed by dissolution–reprecipitation, replacement alteration and solid-state recrystallization. In combination, these various lines of evidence suggest that the composite granite–quartz veins were precipitated from hybrid fluids—hydrous melt and aqueous fluid, respectively—derived by blending primary fluids generated in eclogite and gneiss at UHP conditions that had separated into two immiscible fluid phases during exhumation, as discussed in the next section.

5.2.3 | Constraints on the formation of the composite veins

The *P–T* evolution of the central Sulu belt is summarized in Figure 16. The prograde to peak *P–T* path is based on data in Wang et al. (2016) and Wang et al. (2014); the estimated peak UHP conditions were well in excess of the SCE for crustal compositions (Figure 16). The presence of intergranular coesite in eclogite and the relict igneous mineralogy of the gabbro and gneiss at Yangkou only 2 km to the north of General's Hill (Liou & Zhang, 1996; Wallis et al., 1997; Wang, Kusky, & Li, 2010; Zhang & Liou, 1997), and the relict igneous textures in the gneisses in this study indicate that at the metamorphic peak these rocks were very likely fluid absent (cf. Mosenfelder, Schertl, Smyth, & Liou, 2005; Young & Kylander-Clark, 2015).

Given this fluid absent condition at the metamorphic peak and the likelihood that both eclogite and gneiss have similar total H_2O contents (cf. Chen, Zheng, & Gong, 2011), we infer that during initial decompression under UHP conditions H_2O was exsolved from NAMs in both the eclogite and the gneiss to generate a grain-boundary solute-rich supercritical fluid (cf. Wang et al., 2016). We postulate that as this supercritical fluid increased in volume and solute content with continuing decompression, it created a permeable, interconnected grain boundary network through the solid infrastructure. The formation of this network enabled migration of the supercritical fluid by diffuse porous flow (cf. Turcotte & Ahern, 1978) to form channels, allowing it to pass from one rock type to the other blending compositionally different fluids generated in each rock type. This process brought about the hybrid isotope composition of the ascending fluid as it evolved down pressure to the critical curve.

For low fluid fractions, the ascent velocities for high solute fluids, even in channels, are likely to be slow, decreasing with increasing solute content and viscosity (Hack & Thompson, 2011). Based on the *P–T* range derived from the granite, this supercritical fluid was solute-rich with ~85 wt% solute (based on fig. 1 of Hermann et al., 2013) and granitic in composition, but with higher H_2O content and a viscosity ~3 orders of magnitude lower than granite liquids (Clemens & Petford, 1999). We posit that the slowly ascending supercritical fluid became trapped at a pressure close to that of the critical curve.

The granite in the composite veins has high SiO_2, K_2O, moderate Al_2O_3 and low Na_2O and CaO concentrations, and is enriched in LILE and LREE, but depleted in HFSE and HREE, indicating that it was likely crystallized from a hydrous melt derived from a crustal source (Figure 17). However, when the mineralogy is compared to leucosomes inferred to represent the crystallized products of hydrous melts derived from crustal protoliths (e.g. Lang & Gilotti, 2007; Liu et al., 2010; Wang et al., 2014; Yakymchuk, Brown, Ivanic, & Korhonen, 2013; Yakymchuk et al., 2015), the granite in the composite veins has lower modal feldspar and higher modal quartz, phengite and allanite/epidote. In addition, crystallization occurred at a pressure of 2.5–2.1 GPa, based on phengite barometry, at a

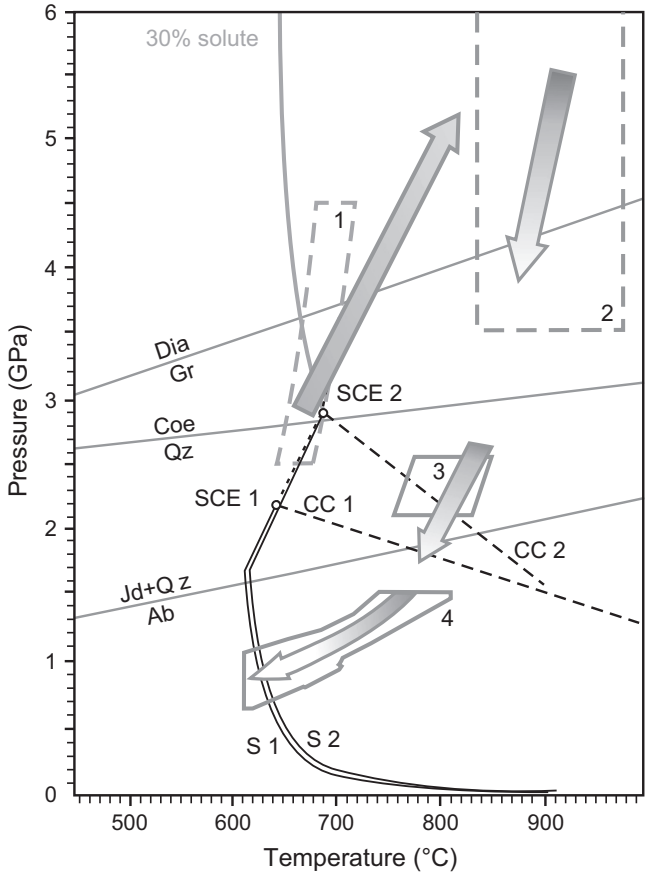

FIGURE 16 Inferred *P–T* path at General's Hill in the central Sulu belt. Dashed boxes 1 and 2 represent Zr-in-rutile temperatures calculated at 2.5–4.5 GPa for rutile inclusions in garnet (from Wang et al., 2016) and the range of peak Grt–Cpx temperatures calculated at 3.5–6 GPa (from Wang et al., 2014), respectively, for UHP eclogite. Solid box 3 shows the range of Ti-in-zircon temperatures calculated at 2.5–2.1 GPa for granite from the composite veins (this study). Solid box 4 represents the calculated *P–T* conditions for phengite breakdown melting in the granite and melt crystallization (from Figure 15). The solid black curves denotes the wet solidi for haplogranite (no CaO; S 1) and Ca-bearing granite (CaO of 1.93 wt%, plagioclase An_{20}; S 2), which terminate at the second critical endpoints (SCE 1 and SCE 2, respectively); the critical curves (CC 1 and CC 2, respectively) extend to lower pressure and higher temperature (from Hack et al., 2007). The uncertainty on the pressure of the critical curves is ±0.2 GPa (Bureau & Keppler, 1999). Arrows show possible late prograde to peak and retrograde *P–T* path segments consistent with the thermobarometric data. Mineral names are abbreviated according to Whitney and Evans (2010)

temperature of ~850–760°C, based on Ti-in-zircon thermometry for the calculated pressure range (Figure 16). Thus, the granite crystallized at temperatures well above the wet solidus at HP metamorphic conditions in the vicinity of the experimentally determined critical curve for Ca-bearing granite, which is similar in composition to the granite in the composite veins [CaO of 1.47 wt% (n = 5) *v.* 1.93 wt% in the experiments of Bureau & Keppler, 1999].

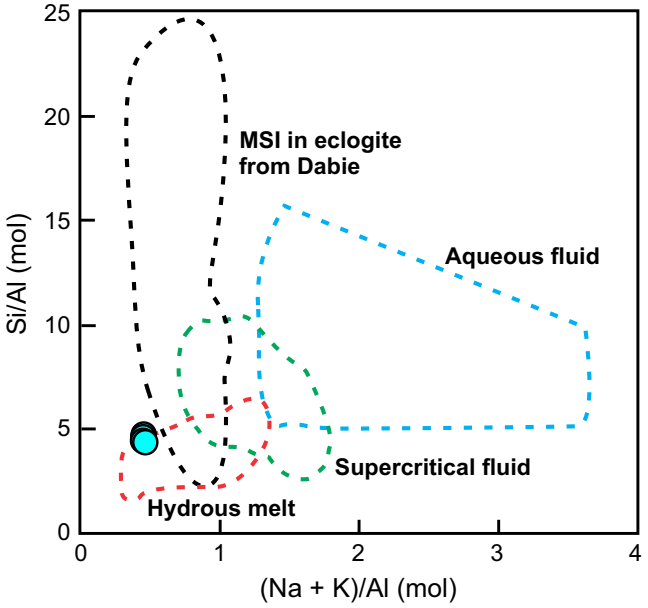

FIGURE 17 Granites from the composite veins shown on the molar SiO_2/Al_2O_3 *v.* molar $(Na_2O+K_2O)/Al_2O_3$ diagram of Hermann et al. (2013), modified by the addition of a field for multiphase solid inclusions (MSI) from data in Gao et al. (2013). The granites plot in the field of hydrous melt

By contrast, the composition of the vein quartz in the composite veins is mostly SiO_2, with very low abundances of other oxides and all trace elements, consistent with precipitation from an aqueous fluid (cf. Hermann et al., 2006).

The strong retrogression of eclogite against the composite veins suggests that crystallization of the veins could have been due to loss of H_2O by diffusion along a gradient in chemical potential between the solute-rich supercritical fluid and the relatively anhydrous eclogite (cf. White & Powell, 2010). As exhumation continued, the supercritical fluid crossed the solvus for the granite–H_2O system, allowing separation into hydrous melt and aqueous fluid at a pressure/temperature determined by the intersection of the bulk composition with the solvus. Thus, the granite and vein quartz were crystallized from hydrous melt and aqueous fluid, respectively, though the parent of these phases was a supercritical fluid formed at much higher pressure during exhumation from UHP conditions. As our study demonstrates, exhumation is a highly dynamic process in which both solid and fluid compositions and proportions change with the evolving *P–T* conditions.

5.3 | Partial melting of the granite in the composite veins during ongoing exhumation of the continental crust

Partial melting during exhumation of UHP rocks has been widely proposed in several orogenic belts (see reviews by

Hermann & Rubatto, 2014; Zheng & Hermann, 2014), where it is inferred to have been triggered mainly by breakdown of hydrous minerals, including phengite and zoisite (Auzanneau, Vielzeuf, & Schmidt, 2006; Hermann & Spandler, 2008; Liu, Jin, & Zhang, 2009; Liu, Hermann, & Zhang, 2013; Schmidt, Vielzeuf, & Auzanneau, 2004; Skjerlie & Douce, 2002). Microstructural evidence in the granite from the composite veins—aggregates of biotite+plagioclase+K-feldspar at the edges of phengite and thin films, cuspate veinlets and patches of K-feldspar along grain boundaries (Figure 4e–i)—are consistent with the former presence of an intergranular melt (Holness, Cesare, & Sawyer, 2011; Sawyer, 1999; Vernon, 2011). Consequently, we interpret K-feldspar in the granite to be largely a product of low volume partial melting due to phengite breakdown. Similar microstructures are also present in the gneiss (Figure 5f). These features suggest that during exhumation from HP eclogite to amphibolite facies conditions (Figure 16), minor phengite-breakdown melting occurred in both the granite and the gneiss. The microstructures are consistent with the sequence of phase assemblage fields in the *P–T* pseudosection calculated for the composition of the granite from a composite vein and discussed above (Figure 15). Thus, we propose a low-*P* retrograde *P–T* path similar to the exemplar white arrow (Figure 15), with final melt crystallization recording conditions of 0.7–1.1 GPa and <670 °C.

5.4 | Implications for multistage fluid interactions between continental crust and mantle in the subduction channel

Subduction zones are important sites for the exchange of mass and energy between the mantle and crust (e.g. Brown & Rushmer, 2006; Hermann et al., 2006; Huangfu, Wang, Li, Fan & Zhang, 2016; Mibe et al., 2011; Zheng, 2012). Although arc magmatism generally does not accompany continental subduction (Rumble, Liou, & Jahn, 2003; Zheng, 2012), the development of syn-exhumation and post-collisional magmatic rocks with distinct chemical signatures indicates that crust–mantle interactions nonetheless occur during continental subduction and exhumation (Dai, Zhao, Zheng, & Zhang, 2015; Guo, Fan, Wang, & Zhang, 2004; Zhao, Dai, & Zheng, 2013; Zhao et al., 2012).

In this study, we have shown that composite granite–quartz veins formed during phase separation of supercritical fluid as it crossed the critical curve around the transition from UHP to HP metamorphic conditions, and that the granite in these veins experienced minor phengite-breakdown melting during ongoing exhumation. This represents a rare natural example of the variety of fluids that could be transferred to the subduction channel to interact with the mantle wedge during exhumation of continental crust from UHP metamorphic conditions.

The importance of a crustal component in the mantle at UHP pressures is supported, for example, by information from majorite-hosted diamond-bearing multiphase solid inclusions in websterite from the island of Fjørtoft in the northernmost UHP terrane of the Western Gneiss Region of Norway (Table S1; Carswell & van Roermund, 2005; Malaspina et al., 2010; van Roermund et al., 2002). Here, the multiphase solid inclusions were interpreted to have precipitated from an oxidized supercritical fluid derived from the deeply subducted continental crust that infiltrated into the mantle wedge at depths ≥130 km.

6 | CONCLUSIONS

This study of composite granite–quartz veins in eclogite provides new information that contributes to our growing understanding of the origin and evolution of supercritical fluid during exhumation of deeply subducted continental crust. We posit that eclogite and gneiss at General's Hill in the central Sulu belt were likely fluid absent at the peak of UHP metamorphism, and argue that a supercritical fluid was generated by exsolution of H_2O stored in NAMs during exhumation from the peak UHP conditions. This fluid migrated by diffuse porous flow into channels enabling it to pass from one fluid source to another. This conclusion is supported by a variety of isotope data that require the supercritical fluid to be a hybrid derived by mixing of fluids produced in both eclogite and gneiss.

The blended supercritical fluid evolved by dissolution of the silicate mineral matrix, becoming increasingly solute-rich and 'granitic' until it became trapped. As crystallization began by diffusive loss of H_2O to the host eclogite concomitant with ongoing exhumation of the crust, the trapped supercritical fluid intersected the solvus for the granite–H_2O system, allowing phase separation and formation of the composite veins. Subsequently, the granite in the composite veins and the surrounding gneisses experienced minor partial melting due to phengite breakdown during exhumation from HP eclogite to amphibolite facies *P–T* conditions.

The results of this study demonstrate that different fluid phases were available successively in continental crust undergoing exhumation after ultradeep subduction, changing from supercritical fluid at UHP conditions to coexisting hydrous melt and aqueous fluid at HP conditions, and then hydrous melt derived by hydrate-breakdown at lower pressures. This succession shows that the crustal component that may interact with the mantle at the slab–mantle interface evolves with changing *P–T* conditions. Thus, supercritical fluid is dominant at UHP conditions, whereas

hydrous melts play the major role at shallower depths in the subduction channel.

ACKNOWLEDGEMENTS

The first author Song-Jie Wang is grateful to the China Scholarship Council for funding a 12-month PhD joint supervision at the University of Maryland, College Park (CSC no. 201506410003). This research was funded by the National Natural Science Foundation of China (nos 41272225, 41572182) and the Fundamental Research Funds for National University, China University of Geosciences, Wuhan (no. CUG–G1323511572); the WiscSIMS Laboratory is funded by the US National Science Foundation (EAR03-19230, EAR10-53466, EAR13-55590). We thank Y.S. Liu and Z.C. Hu for help with LA(MC)-ICP-MS analysis, H.H. Chen for help with whole-rock trace element analysis, L. Zhou for help with whole-rock Sr–Nd isotope analysis, J. Valley, J. Kern and A. Ishida for assistance with SIMS analysis, and B. Hess for sample preparation. We acknowledge Y.B. Wu, M. Tang and H. Yang for useful suggestions concerning interpretation of the geochemical data, three anonymous reviewers for insightful comments and K. Evans for editorial advice.

REFERENCES

Audétat, A., & Keppler, H. (2004). Viscosity of fluids in subduction zones. *Science*, *303*, 513–516.

Auzanneau, E., Vielzeuf, D., & Schmidt, M. W. (2006). Experimental evidence of decompression melting during exhumation of subducted continental crust. *Contributions to Mineralogy and Petrology*, *152*, 125–148.

Bebout, G. E. (2014). Chemical and isotopic cycling in subduction zones. *Treatise on Geochemistry*, *4*, 703–747.

Bebout, G. E., & Penniston-Dorland, S. C. (2016). Fluid and mass transfer at subduction interfaces—The field metamorphic record. *Lithos*, *240*, 228–258.

Brown, M. (2014). The contribution of metamorphic petrology to understanding lithosphere evolution and geodynamics. *Geoscience Frontiers*, *5*, 553–569.

Brown, M., Korhonen, F. J., & Siddoway, C. S. (2011). Organizing melt flow through the crust. *Elements*, *7*, 261–266.

Brown, M., & Rushmer, T. (2006). *Evolution and differentiation of the continental crust*. Cambridge, UK: Cambridge University Press.

Bureau, H., & Keppler, H. (1999). Complete miscibility between silicate melts and hydrous fluids in the upper mantle: Experimental evidence and geochemical implications. *Earth and Planetary Science Letters*, *165*, 187–196.

Caddick, M. J., & Thompson, A. B. (2008). Quantifying the tectono-metamorphic evolution of pelitic rocks from a wide range of tectonic settings: Mineral compositions in equilibrium. *Contributions to Mineralogy and Petrology*, *156*, 7–195.

Carswell, D. A., & van Roermund, H. L. (2005). On multi-phase mineral inclusions associated with microdiamond formation in mantle-derived peridotite lens at Bardane on Fjørtoft, west Norway. *European Journal of Mineralogy*, *17*, 31–42.

Chen, B., Ye, K., & Liu, J. (2002). Cogenetic relationship of the Yangkou gabbro-to-granite unit, Su-Lu terrane, eastern China, and implications for UHP metamorphism. *Journal of the Geological Society*, *159*, 457–467.

Chen, Y. X., Zheng, Y. F., Chen, R. X., Zhang, S.B., Li, Q.L., Dai, M.N, … Chen, L. (2011). Metamorphic growth and recrystallization of zircons in extremely ^{18}O-depleted rocks during eclogite-facies metamorphism: Evidence from U–Pb ages, trace elements, and O–Hf isotopes. *Geochimica et Cosmochimica Acta*, *75*, 4877–4898.

Chen, R. X., Zheng, Y. F., & Gong, B. (2011). Mineral hydrogen isotopes and water contents in ultrahigh-pressure metabasite and metagranite: Constraints on fluid flow during continental subduction-zone metamorphism. *Chemical Geology*, *281*, 103–124.

Chen, R. X., Zheng, Y. F., & Hu, Z. C. (2012). Episodic fluid action during exhumation of deeply subducted continental crust: Geochemical constraints from zoisite–quartz vein and host metabasite in the Dabie orogen. *Lithos*, *155*, 146–166.

Chen, Y. X., Zheng, Y. F., & Hu, Z. C. (2013). Petrological and zircon evidence for anatexis of UHP quartzite during continental collision in the Sulu orogen. *Journal of Metamorphic Geology*, *31*, 389–413.

Chen, Y. X., Zheng, Y. F., Li, L., & Chen, R. X. (2014). Fluid-rock interaction and geochemical transport during protolith emplacement and continental collision: A tale from Qinglongshan ultrahigh-pressure metamorphic rocks in the Sulu orogen. *American Journal of Sciences*, *314*, 357–399.

Chen, R. X., Zheng, Y. F., & Xie, L. (2010). Metamorphic growth and recrystallization of zircon: Distinction by simultaneous in-situ analyses of trace elements, U-Th–Pb and Lu–Hf isotopes in zircons from eclogite-facies rocks in the Sulu orogen. *Lithos*, *114*, 132–154.

Cherniak, D. J., & Watson, E. B. (2007). Ti diffusion in zircon. *Chemical Geology*, *242*, 473–483.

Clemens, J. D., & Petford, N. (1999). Granitic melt viscosity and silicic magma dynamics in contrasting tectonic settings. *Journal of the Geological Society*, *156*, 1057–1060.

Corfu, F., Hanchar, J. M., Hoskin, P. W., & Kinny, P. (2003). Atlas of zircon textures. *Reviews in Mineralogy and Geochemistry*, *53*, 469–500.

Dai, L. Q., Zhao, Z. F., Zheng, Y. F., & Zhang, J. (2015). Source and magma mixing processes in continental subduction factory: Geochemical evidence from postcollisional mafic igneous rocks in the Dabie orogen. *Geochemistry, Geophysics, Geosystems*, *16*, 659–680.

Eiler, J. M. (2001). Oxygen isotope variations of basaltic lavas and upper mantle rocks. *Reviews in Mineralogy and Geochemistry*, *43*, 319–364.

Ernst, W., Tsujimori, T., Zhang, R. Y., & Liou, J. G. (2007). Permo-Triassic collision, subduction-zone metamorphism, and tectonic exhumation along the East Asian continental margin. *Annual Review of Earth and Planetary Sciences*, *35*, 73–110.

Ferrando, S., Frezzotti, M., Dallai, L., & Compagnoni, R. (2005). Multiphase solid inclusions in UHP rocks (Su-Lu, China): Remnants of supercritical silicate-rich aqueous fluids released during continental subduction. *Chemical Geology*, *223*, 68–81.

Ferrando, S., Frezzotti, M. L., Petrelli, M., & Compagnoni, R. (2009). Metasomatism of continental crust during subduction: The UHP whiteschists from the Southern Dora-Maira Massif (Italian Western Alps). *Journal of Metamorphic Geology*, *27*, 739–756.

Ferrero, S., Wunder, B., Walczak, K., O'Brien, P. J., & Ziemann, M. A. (2015). Preserved near ultrahigh-pressure melt from continental crust subducted to mantle depths. *Geology*, *43*(5), 447–450.

Ferry, J. M., & Watson, E. B. (2007). New thermodynamic models and revised calibrations for the Ti-in-zircon and Zr-in-rutile thermometers. *Contributions to Mineralogy and Petrology*, *154*, 429–437.

Frezzotti, M. L., & Ferrando, S. (2015). The chemical behavior of fluids released during deep subduction based on fluid inclusions. *American Mineralogist*, *100*, 352–377.

Frezzotti, M. L., Ferrando, S., Dallai, L., & Compagnoni, R. (2007). Intermediate alkali–alumino-silicate aqueous solutions released by deeply subducted continental crust: Fluid evolution in UHP OH-Rich topaz–kyanite quartzites from Donghai (Sulu, China). *Journal of Petrology*, *48*, 1219–1241.

Gao, J., & Klemd, R. (2001). Primary fluids entrapped at blueschist to eclogite transition: Evidence from the Tianshan meta-subduction complex in northwestern China. *Contributions to Mineralogy and Petrology*, *142*, 1–14.

Gao, X. Y., Zheng, Y. F., Chen, Y. X., & Hu, Z. C. (2013). Trace element composition of continentally subducted slab-derived melt: Insight from multiphase solid inclusions in ultrahigh-pressure eclogite in the Dabie orogen. *Journal of Metamorphic Geology*, *31*, 453–468.

Gao, X. Y., Zheng, Y. F., Xia, X. P., & Chen, Y. X. (2014). U-Pb ages and trace elements of metamorphic rutile from ultrahigh-pressure quartzite in the Sulu orogen. *Geochimica et Cosmochimica Acta*, *143*, 87–114.

Gerya, T., & Meilick, F. (2011). Geodynamic regimes of subduction under an active margin: Effects of rheological weakening by fluids and melts. *Journal of Metamorphic Geology*, *29*, 7–31.

Gong, B., Chen, R. X., & Zheng, Y. F. (2013). Water contents and hydrogen isotopes in nominally anhydrous minerals from UHP metamorphic rocks in the Dabie-Sulu orogenic belt. *Chinese Science Bulletin*, *58*, 4384–4389.

Green, E. C. R., White, R. W., Diener, J. F. A., Powell, R., & Holland, T. J. B. (2016). Activity–composition relations for the calculation of partial melting equilibria in metabasic rocks. *Journal of Metamorphic Geology*, *34*, 845–869.

Guo, S., Chen, Y., Ye, K., Su, B., Yang, Y.H., Zhang, L.M., … Mao, Q. (2015). Formation of multiple high-pressure veins in ultrahigh-pressure eclogite (Hualiangting, Dabie terrane, China): Fluid source, element transfer, and closed-system metamorphic veining. *Chemical Geology*, *417*, 238–260.

Guo, F., Fan, W., Wang, Y., & Zhang, M. (2004). Origin of early Cretaceous calc-alkaline lamprophyres from the Sulu orogen in eastern China: Implications for enrichment processes beneath continental collisional belt. *Lithos*, *78*, 291–305.

Guo, X., Wang, Y., Liu, H., & Zi, J. (2016). Zircon U-Pb geochronology of the Cenozoic granitic mylonite along the Ailaoshan-Red river shear zone: New constraints on the timing of the sinistral shearing. *Journal of Earth Science*, *27*(3), 435–443.

Hack, A. C., & Thompson, A. B. (2011). Density and viscosity of hydrous magmas and related fluids and their role in subduction zone processes. *Journal of Petrology*, *52*, 1333–1362.

Hack, A. C., Thompson, A. B., & Aerts, M. (2007). Phase relations involving hydrous silicate melts, aqueous fluids, and minerals. *Reviews in Mineralogy and Geochemistry*, *65*, 129–185.

Hacker, B. R., Ratschbacher, L., Webb, L., McWilliams Ireland, T., Calvert, A., … Chateigner, D. (2000). Exhumation of ultrahigh-pressure continental crust in east central China: Late Triassic-Early Jurassic tectonic unroofing. *Journal of Geophysical Research: Solid Earth*, *105*, 13339–13364.

Hayden, L. A., & Manning, C. E. (2011). Rutile solubility in supercritical $NaAlSi_3O_8$–H_2O fluids. *Chemical Geology*, *284*, 74–81.

Hayden, L. A., & Watson, E. B. (2007). Rutile saturation in hydrous siliceous melts and its bearing on Ti-thermometry of quartz and zircon. *Earth and Planetary Science Letters*, *258*, 561–568.

He, Q., Zhang, S. B., & Zheng, Y. F. (2016). High temperature glacial meltwater-rock reaction in the Neoproterozoic: Evidence from zircon in-situ oxygen isotopes in granitic gneiss from the Sulu orogen. *Precambrian Research*, *284*, 1–13.

Hermann, J., & Rubatto, D. (2014). Subduction of continental crust to mantle depth: Geochemistry of ultrahigh-pressure rocks. *Treatise on Geochemistry*, *4*, 309–340.

Hermann, J., & Spandler, C. J. (2008). Sediment melts at sub-arc depths: An experimental study. *Journal of Petrology*, *49*, 717–740.

Hermann, J., Spandler, C., Hack, A., & Korsakov, A. V. (2006). Aqueous fluids and hydrous melts in high-pressure and ultra-high pressure rocks: Implications for element transfer in subduction zones. *Lithos*, *92*, 399–417.

Hermann, J., Zheng, Y. F., & Rubatto, D. (2013). Deep fluids in subducted continental crust. *Elements*, *9*, 281–287.

Holland, T., & Powell, R. (2001). Calculation of phase relations involving haplogranitic melts using an internally consistent thermodynamic dataset. *Journal of Petrology*, *42*, 673–683.

Holland, T. J. B., & Powell, R. (2011). An improved and extended internally consistent thermodynamic dataset for phases of petrological interest, involving a new equation of state for solids. *Journal of Metamorphic Geology*, *29*, 333–383.

Holness, M. B., Cesare, B., & Sawyer, E. W. (2011). Melted rocks under the microscope: Microstructures and their interpretation. *Elements*, *7*, 247–252.

Hoskin, P. W. (2005). Trace-element composition of hydrothermal zircon and the alteration of Hadean zircon from the Jack Hills, Australia. *Geochimica et Cosmochimica Acta*, *69*, 637–648.

Hoskin, P. W., & Ireland, T. R. (2000). Rare earth element chemistry of zircon and its use as a provenance indicator. *Geology*, *28*, 627–630.

Huangfu, P., Wang, Y., Li, Z., Fan, W. & Zhang, Y. (2016). Effects of crustal eclogitization on plate subduction/collision dynamics: Implications for India-Asia collision. *Journal of Earth Science*, *27* (5), 727–739.

Kawamoto, T., Kanzaki, M., Mibe, K., Matsukage, K. N., & Ono, S. (2012). Separation of supercritical slab-fluids to form aqueous fluid and melt components in subduction zone magmatism. *Proceedings of the National Academy of Sciences*, *109*, 18695–18700.

Kawamoto, T., Mibe, K., Bureau, H., Reguer, S., Mocuta, C., Kubsky, S., … Kogiso, T. (2014). Large-ion lithophile elements delivered by saline fluids to the sub-arc mantle. *Earth, Planets and Space*, *66*, 1–11.

Keppler, H. (2017). Fluids and trace element transport in subduction zones. *American Mineralogist*, *102*, 5–20.

Kessel, R., Schmidt, M. W., Ulmer, P., & Pettke, T. (2005). Trace element signature of subduction-zone fluids, melts and supercritical liquids at 120–180 km depth. *Nature*, *437*, 724–727.

Labrousse, L., Duretz, T., & Gerya, T. (2015). H_2O-fluid-saturated melting of subducted continental crust facilitates exhumation of ultrahigh-pressure rocks in continental subduction zones. *Earth and Planetary Science Letters*, *428*, 151–161.

Labrousse, L., Prouteau, G., & Ganzhorn, A. C. (2011). Continental exhumation triggered by partial melting at ultrahigh pressure. *Geology*, *39*, 1171–1174.

Lang, H., & Gilotti, J. (2007). Partial melting of metapelites at ultra-high-pressure conditions, Greenland Caledonides. *Journal of Metamorphic Geology*, *25*, 129–147.

Li, Z. X., Li, X., Kinny, P., Wang, J., Zhang, S., & Zhou, H. (2003). Geochronology of Neoproterozoic syn-rift magmatism in the Yangtze Craton, South China and correlations with other continents: Evidence for a mantle superplume that broke up Rodinia. *Precambrian Research*, *122*, 85–109.

Li, X. P., Zheng, Y. F., Wu, Y. B., Chen, F., Gong, B., & Li, Y. L. (2004). Low-T eclogite in the Dabie terrane of China: Petrological and isotopic constraints on fluid activity and radiometric dating. *Contributions to Mineralogy and Petrology*, *148*, 443–470.

Liou, J. G., Ernst, W., Zhang, R., Tsujimori, T., & Jahn, B. (2009). Ultrahigh-pressure minerals and metamorphic terranes – The view from China. *Journal of Asian Earth Sciences*, *35*, 199–231.

Liou, J. G., & Zhang, R. Y. (1996). Occurrences of intergranular coesite in ultrahigh-P rocks from the Sulu region, eastern China: Implications for lack of fluid during exhumation. *American Mineralogist*, *81*, 1217–1221.

Liou, J. G., Zhang, R. Y., Liu, F. L., Zhang, Z. M., & Ernst, W. G. (2012). Mineralogy, petrology, U-Pb geochronology, and geologic evolution of the Dabie-Sulu classic ultrahigh-pressure metamorphic terrane, East-Central China. *American Mineralogist*, *97*, 1533–1543.

Liu, F. L., Gerdes, A., Liou, J. G., Xue, H. M., & Liang, F. H. (2006). SHRIMP U-Pb zircon dating from Sulu-Dabie dolomitic marble, eastern China: Constraints on prograde, ultrahigh-pressure and retrograde metamorphic ages. *Journal of Metamorphic Geology*, *24*, 569–589.

Liu, Q., Hermann, J. & Zhang, J. (2013). Polyphase inclusions in the Shuanghe UHP eclogites formed by subsolidus transformation and incipient melting during exhumation of deeply subducted crust. *Lithos*, *177*, 91–109.

Liu, D. Y., Jian, P., Kröner, A., & Xu, S. T. (2006). Dating of prograde metamorphic events deciphered from episodic zircon growth in rocks of the Dabie-Sulu UHP complex, China. *Earth and Planetary Science Letters*, *250*, 650–666.

Liu, Q., Jin, Z. M., & Zhang, J. F. (2009). An experimental study of dehydration melting of phengite-bearing eclogite at 1.5–3.0 GPa. *Chinese Science Bulletin*, *54*, 2090–2100.

Liu, F. L., & Liou, J. G. (2011). Zircon as the best mineral for P-T–time history of UHP metamorphism: A review on mineral inclusions and U–Pb SHRIMP ages of zircons from the Dabie-Sulu UHP rocks. *Journal of Asian Earth Sciences*, *40*, 1–39.

Liu, F. L., Robinson, P. T., Gerdes, A., Xue, H., Liu, P., & Liou, J. G. (2010). Zircon U-Pb ages, REE concentrations and Hf isotope compositions of granitic leucosome and pegmatite from the north Sulu UHP terrane in China: Constraints on the timing and nature of partial melting. *Lithos*, *117*, 247–268.

Liu, X. C., Wu, Y. B., Gao, S., Wang, H., Zheng, J.P., Hu, Z.C., … Yang, S.H. (2014). Record of multiple stage channelized fluid and melt activities in deeply subducted slab from zircon U-Pb age and Hf–O isotope compositions. *Geochimica et Cosmochimica Acta*, *144*, 1–24.

Liu, F. L., Xu, Z. Q., & Liou, J. G. (2004). Tracing the boundary between UHP and HP metamorphic belts in the southwestern Sulu terrane, eastern China: Evidence from mineral inclusions in zircons from metamorphic rocks. *International Geological Review*, *46*, 409–425.

Malaspina, N., Scambelluri, M., Poli, S., van Roermund, H. L. M., & Langenhorst, F. (2010). The oxidation state of mantle wedge majoritic garnet websterites metasomatised by C-bearing subduction fluids. *Earth and Planetary Science Letters*, *298*, 417–426.

Manning, C. E. (2004). The chemistry of subduction-zone fluids. *Earth and Planetary Science Letters*, *223*, 1–16.

Martin, C., & Duchêne, S. (2015). Residual water in hydrous minerals as a kinetic factor for omphacite destabilization into symplectite in the eclogites of Vardalsneset (WGR, Norway). *Lithos*, *232*, 162–173.

Mibe, K., Kawamoto, T., Matsukage, K. N., Fei, Y., & Ono, S. (2011). Slab melting versus slab dehydration in subduction-zone magmatism. *Proceedings of the National Academy of Sciences*, *108*, 8177–8182.

Mosenfelder, J. L., Schertl, H. P., Smyth, J. R., & Liou, J. G. (2005). Factors in the preservation of coesite: The importance of fluid infiltration. *American Mineralogist*, *90*, 779–789.

O'Neil, J., & Chappell, B. (1977). Oxygen and hydrogen isotope relations in the Berridale batholith. *Journal of the Geological Society*, *133*, 559–571.

Philippot, P., & Selverstone, J. (1991). Trace-element-rich brines in eclogitic veins: Implications for fluid composition and transport during subduction. *Contributions to Mineralogy and Petrology*, *106*, 417–430.

Powell, R., & Holland, T. J. B. (1988). An internally consistent dataset with uncertainties and correlations: 3. Applications to geobarometry, worked examples and a computer program. *Journal of Metamorphic Geology*, *6*(2), 173–204.

Rosenberg, C. L., & Handy, M. R. (2005). Experimental deformation of partially melted granite revisited: Implications for the continental crust. *Journal of Metamorphic Geology*, *23*, 19–28.

Rubatto, D. (2002). Zircon trace element geochemistry: Partitioning with garnet and the link between U–Pb ages and metamorphism. *Chemical Geology*, *184*, 123–138.

Rubatto, D., & Hermann, J. (2003). Zircon formation during fluid circulation in eclogites (Monviso, Western Alps): Implications for Zr and Hf budget in subduction zones. *Geochimica et Cosmochimica Acta*, *67*, 2173–2187.

Rubatto, D., & Hermann, J. (2007). Zircon behaviour in deeply subducted rocks. *Elements*, *3*, 31–35.

Rumble, D., Liou, J. G., & Jahn, B. M. (2003). Continental crust subduction and ultrahigh pressure metamorphism. *Treatise on Geochemistry*, *3*, 293–319.

Sawyer, E. (1999). Criteria for the recognition of partial melting. *Physics and Chemistry of the Earth, Part A: Solid Earth and Geodesy*, *24*, 269–279.

Scambelluri, M., Pettke, T., & van Roermund, H. (2008). Majoritic garnets monitor deep subduction fluid flow and mantle dynamics. *Geology*, *36*, 59–62.

Scambelluri, M., & Philippot, P. (2001). Deep fluids in subduction zones. *Lithos*, *55*, 213–227.

Schertl, H. P., & O'Brien, P. J. (2013). Continental crust at mantle depths: Key minerals and microstructures. *Elements*, *9*, 261–266.

Schmidt, M. W., & Poli, S. (2014). Devolatilization during subduction. In H. D. Holland & K. K. Turekian (Eds.), *The crust, treatise on geochemistry*, (vol. 4, 2nd ed., pp. 669–701). Oxford: Elsevier-Pergamon.

Schmidt, M. W., Vielzeuf, D., & Auzanneau, E. (2004). Melting and dissolution of subducting crust at high pressures: The key role of white mica. *Earth and Planetary Science Letters*, *228*, 65–84.

Sheng, Y. M., Zheng, Y. F., Chen, R. X., Li, Q., & Dai, M. (2012). Fluid action on zircon growth and recrystallization during quartz veining within UHP eclogite: Insights from U-Pb ages, O–Hf isotopes and trace elements. *Lithos*, *136*, 126–144.

Sheng, Y. M., Zheng, Y. F., Li, S. N., & Hu, Z. (2013). Element mobility during continental collision: Insights from polymineralic metamorphic vein within UHP eclogite in the Dabie orogen. *Journal of Metamorphic Geology*, *31*, 221–241.

Sizova, E., Gerya, T., & Brown, M. (2012). Exhumation mechanisms of melt-bearing ultrahigh pressure crustal rocks during collision of spontaneously moving plates. *Journal of Metamorphic Geology*, *30*, 927–955.

Skjerlie, K. P., & Douce, A. E. P. (2002). The fluid-absent partial melting of a zoisite-bearing quartz eclogite from 1.0 to 3.2 GPa: Implications for melting in thickened continental crust and for subduction-zone processes. *Journal of Petrology*, *43*, 291–314.

Spandler, C., & Hermann, J. (2006). High-pressure veins in eclogite from New Caledonia and their significance for fluid migration in subduction zones. *Lithos*, *89*, 135–153.

Spandler, C., Pettke, T., & Rubatto, D. (2011). Internal and external fluid sources for eclogite-facies veins in the Monviso meta-ophiolite, Western Alps: Implications for fluid flow in subduction zones. *Journal of Petrology*, *52*, 1207–1236.

Spandler, C., & Pirard, C. (2013). Element recycling from subducting slabs to arc crust: A review. *Lithos*, *170*, 208–223.

Stöckhert, B., Duyster, J., Trepmann, C., & Massonne, H. J. (2001). Microdiamond daughter crystals precipitated from supercritical COH+ silicate fluids included in garnet, Erzgebirge, Germany. *Geology*, *29*, 391–394.

Stöckhert, B., Trepmann, C., & Massonne, H. J. (2009). Decrepitated UHP fluid inclusions: About diverse phase assemblages and extreme decompression rates (Erzgebirge, Germany). *Journal of Metamorphic Geology*, *27*, 673–684.

Sun, S. S., & McDonough, W. F. (1989). Chemical and isotopic systematics of oceanic basalts: Implications for mantle composition and processes. *Geological Society, London, Special Publications*, *42*, 313–345.

Tang, J., Zheng, Y. F., Gong, B., Wu, Y. B., Gao, T. S., Yuan, H. L., … Wu, F. Y. (2008). Extreme oxygen isotope signature of meteoric water in magmatic zircon from metagranite in the Sulu orogen, China: Implications for Neoproterozoic rift magmatism. *Geochimica et Cosmochimica Acta*, *72*, 3139–3169.

Turcotte, D. L., & Ahern, J. L. (1978). A porous flow model for magma migration in the asthenosphere. *Journal of Geophysical Research*, *83*(B2), 767–772.

Valley, J. W., Kinny, P. D., Schulze, D. J., & Spicuzza, M. J. (1998). Zircon megacrysts from kimberlite: Oxygen isotope variability among mantle melts. *Contributions to Mineralogy and Petrology*, *133*, 1–11.

Valley, J. W., Lackey, J. S., Cavosie, A. J., Clechenko, C. C., Spicuzza, M. J., Basei, M. A. S., … Peck, W. H. (2005). 4.4 billion years of crustal maturation: oxygen isotope ratios of magmatic zircon. *Contributions to Mineralogy and Petrology*, *150*(6), 561–580.

van Roermund, H. L., Carswell, D. A., Drury, M. R., & Heijboer, T. C. (2002). Microdiamonds in a megacrystic garnet websterite pod from Bardane on the island of Fjørtoft, western Norway: Evidence for diamond formation in mantle rocks during deep continental subduction. *Geology*, *30*, 959–962.

Verlaguet, A., Goffé, B., Brunet, F., Poinssot, C., Vidal, O., Findling, N., … Menut, D. (2011). Metamorphic veining and mass transfer in a chemically closed system: a case study in Alpine metabauxites (western Vanoise). *Journal of Metamorphic Geology*, *29*(3), 275–300.

Vernon, R. (2011). Microstructures of melt-bearing regional metamorphic rocks. *Geological Society of America Memoirs*, *207*, 1–11.

Vrijmoed, J. C., Smith, D. C., & van Roermund, H. L. M. (2008). Raman confirmation of microdiamond in the Svartberget Fe-Ti type garnet peridotite, Western Gneiss Region, Western Norway. *Terra Nova*, *20*, 295–301.

Wallis, S. R., Ishiwatari, A., Hirajima, T., Ye, K., Guo, J., Nakamura, D., … Banno, S. (1997). Occurrence and field relationships of ultrahigh-pressure metagranitoid and coesite eclogite in the Su-Lu terrane, eastern China. *Journal of the Geological Society*, *154*, 45–54.

Wang, L., Kusky, T. M., & Li, S. Z. (2010). Structural geometry of an exhumed UHP terrane in the eastern Sulu Orogen, China: Implications for continental collisional processes. *Journal of Structural Geology*, *32*, 423–444.

Wang, L., Kusky, T. M., Polat, A., Wang, S. J., Jiang, X. F., Zong, K. Q., … Fu, J. M. (2014). Partial melting of deeply subducted eclogite from the Sulu orogen in China. *Nature Communications*, *5*: 5604, 1–11.

Wang, S. J., Wang, L., Brown, M., & Feng, P. (2016). Multi-stage barite crystallization in partially melted UHP eclogite from the Sulu belt, China. *American Mineralogist*, *101*, 564–579.

Watson, E. B., Wark, D. A., & Thomas, J. B. (2006). Crystallization thermometers for zircon and rutile. *Contributions to Mineralogy and Petrology*, *151*, 413–433.

White, R. W., & Powell, R. (2010). Retrograde melt–residue interaction and the formation of near-anhydrous leucosomes in migmatites. *Journal of Metamorphic Geology*, *28*(6), 579–597.

White, R. W., Powell, R., Holland, T. J. B., Johnson, T. E., & Green, E. C. R. (2014). New mineral activity-composition relations for thermodynamic calculations in metapelitic systems. *Journal of Metamorphic Geology*, *32*, 261–286.

White, R. W., Powell, R., & Johnson, T. E. (2014). The effect of Mn on mineral stability in metapelites revisited: New *a–x* relations for manganese-bearing minerals. *Journal of Metamorphic Geology*, *32*, 809–828.

Whitehouse, M. J., & Platt, J. P. (2003). Dating high-grade metamorphism—Constraints from rare-earth elements in zircon and garnet. *Contributions to Mineralogy and Petrology*, *145*, 61–74.

Whitney, D. L., & Evans, B. W. (2010). Abbreviations for names of rock-forming minerals. *American Mineralogist*, *95*, 185.

Wu, Y. B., Gao, S., Zhang, H. F., Yang, S. H., Liu, X. C., Jiao, W. F., … He, M. C. (2009). U–Pb age, trace-element, and Hf-isotope compositions of zircon in a quartz vein from eclogite in the western Dabie Mountains: Constraints on fluid flow during early exhumation of ultrahigh-pressure rocks. *American Mineralogist*, *94*, 303–312.

Wu, Y. B., & Zheng, Y. F. (2004). Genesis of zircon and its constraints on interpretation of U−Pb age. *Chinese Science Bulletin*, *49*, 1554–1569.

Wu, Y. B., Zheng, Y. F., Zhao, Z. F., Gong, B., Liu, X., & Wu, F. Y. (2006). U-Pb, Hf and O isotope evidence for two episodes of fluid-assisted zircon growth in marble-hosted eclogites from the Dabie orogen. *Geochimica et Cosmochimica Acta*, *70*, 3743–3761.

Xia, Q. K., Sheng, Y. M., Yang, X. Z., & Yu, H. M. (2005). Heterogeneity of water in garnets from UHP eclogites, eastern Dabieshan, China. *Chemical Geology*, *224*, 237–246.

Xia, Q. X., Zheng, Y. F., & Hu, Z. C. (2010). Trace elements in zircon and coexisting minerals from low-T/UHP metagranite in the Dabie orogen: Implications for action of supercritical fluid during continental subduction-zone metamorphism. *Lithos*, *114*, 385–412.

Xia, Q. X., Zheng, Y. F., Yuan, H., & Wu, F. Y. (2009). Contrasting Lu–Hf and U-Th–Pb isotope systematics between metamorphic growth and recrystallization of zircon from eclogite-facies metagranites in the Dabie orogen, China. *Lithos*, *112*, 477–496.

Xiong, F., Ma, C., Jiang, H. A., & Zhang, H. (2016). Geochronology and petrogenesis of Triassic high-K calc-alkaline granodiorites in the East Kunlun orogen, West China: Juvenile lower crustal melting during post-collisional extension. *Journal of Earth Science*, *27* (3), 474–490.

Xu, Z. Q., Wang, Q., Ji, S. C., Chen, J., Zeng, L. S., Yang, J. S., … Wenk, H. (2006). Petrofabrics and seismic properties of garnet peridotite from the UHP Sulu terrane (China): Implications for olivine deformation mechanism in a cold and dry subducting continental slab. *Tectonophysics*, *421*, 111–127.

Xu, H. J., Ye, K., Song, Y. R., Chen, Y., Zhang, J. F., Liu, Q., … Guo, S. (2013). Prograde metamorphism, decompressional partial melting and subsequent melt fractional crystallization in the Weihai migmatitic gneisses, Sulu UHP terrane, eastern China. *Chemical Geology*, *341*, 16–37.

Yakymchuk, C., Brown, M., Clark, C., Korhonen, F. J., Piccoli, P. M., Siddoway, C. S., … Vervoort, J. D. (2015). Decoding polyphase migmatites using geochronology and phase equilibria modelling. *Journal of Metamorphic Geology*, *33*, 203–230.

Yakymchuk, C., Brown, M., Ivanic, T., & Korhonen, F. (2013). Leucosome distribution in migmatitic paragneisses and orthogneisses: A record of self-organized melt migration and entrapment in a heterogeneous partially-molten crust. *Tectonophysics*, *603*, 136–154.

Yardley, B. W. D., & Valley, J. W. (1997). The petrologic case for a dry lower crust. *Journal of Geophysical Research: Solid Earth*, *102*, 12173–12185.

Ye, K., Cong, B. L., & Ye, D. N. (2000). The possible subduction of continental material to depths greater than 200 km. *Nature*, *407*, 734–736.

Ye, K., Yao, Y. P., Katayama, I., Cong, B. L., Wang, Q., & Maruyama, S. (2000). Large areal extent of ultrahigh-pressure metamorphism in the Sulu ultrahigh-pressure terrane of East China: New implications from coesite and omphacite inclusions in zircon of granitic gneiss. *Lithos*, *52*, 157–164.

Young, D. J., & Kylander-Clark, A. R. C. (2015). Does continental crust transform during eclogite facies metamorphism? *Journal of Metamorphic Geology*, *33*, 331–357.

Zeng, L. S., Gao, L. E., Yu, J. J., & Hu, G. Y. (2011). SHRIMP zircon U/Pb dating on ultrahigh pressure rocks from Yangkou: Implications for the timing of partial melting in the Sulu UHP metamorphic belt. *Acta Petrologica Sinica*, *27*, 1085–1094 (in Chinese with English abstract).

Zhang, R. Y., & Liou, J. G. (1997). Partial transformation of gabbro to coesite-bearing eclogite from Yangkou, the Sulu terrane, eastern China. *Journal of Metamorphic Geology*, *15*, 183–202.

Zhang, R. Y., Liou, J. G., & Ernst, W. (1995). Ultrahigh-pressure metamorphism and decompressional P−T paths of eclogites and country rocks from Weihai, eastern China. *Island Arc*, *4*, 293–309.

Zhang, R. Y., Liou, J. G., & Ernst, W. (2009). The Dabie-Sulu continental collision zone: A comprehensive review. *Gondwana Research*, *16*, 1–26.

Zhang, Z. M., Shen, K., Sun, W. D., Liu, Y. S., Liou, J. G., Shi, C., … Wang, J. L. (2008). Fluids in deeply subducted continental crust: Petrology, mineral chemistry and fluid inclusion of UHP metamorphic veins from the Sulu orogen, eastern China. *Geochimica et Cosmochimica Acta*, *72*, 3200–3228.

Zhang, Z. M., Xiao, Y. L., Hoefs, J., Liou, J. G., & Simon, K. (2006). Ultrahigh pressure metamorphic rocks from the Chinese continental scientific drilling project: I. Petrology and geochemistry of the main hole (0–2,050 m). *Contributions to Mineralogy and Petrology*, *152*, 421–441.

Zhao, Z. F., Dai, L. Q., & Zheng, Y. F. (2013). Postcollisional mafic igneous rocks record crust-mantle interaction during continental deep subduction. *Scientific Reports*, *3*: 3413, 1-6.

Zhao, Y. J., Wu, Y. B., Liu, X. C., Gao, S., Wang, H., Zheng, J.-P, … Yang, S.-H. (2016). Distinct zircon U-Pb and O–Hf–Nd–Sr isotopic behaviour during fluid flow in UHP metamorphic rocks: Evidence from metamorphic veins and their host eclogite in the Sulu Orogen, China. *Journal of Metamorphic Geology*, *34*, 343–362.

Zhao, Z. F., Zheng, Y. F., Gao, T. S., Wu, Y. B., Chen, B., Chen, F. K., … Wu, F. Y. (2006). Isotopic constraints on age and duration of fluid-assisted high-pressure eclogite-facies recrystallization during exhumation of deeply subducted continental crust in the Sulu orogen. *Journal of Metamorphic Geology*, *24*, 687–702.

Zhao, Z. F., Zheng, Y. F., Zhang, J., Dai, L. Q., Li, Q., & Liu, X. (2012). Syn-exhumation magmatism during continental collision: Evidence from alkaline intrusives of Triassic age in the Sulu orogen. *Chemical Geology*, *328*, 70–88.

Zheng, Y. F. (2009). Fluid regime in continental subduction zones: Petrological insights from ultrahigh-pressure metamorphic rocks. *Journal of the Geological Society*, *166*, 763–782.

Zheng, Y. F. (2012). Metamorphic chemical geodynamics in continental subduction zones. *Chemical Geology*, *328*, 5–48.

Zheng, Y. F., Chen, R. X., & Zhao, Z. F. (2009). Chemical geodynamics of continental subduction-zone metamorphism: Insights from studies of the Chinese Continental Scientific Drilling (CCSD) core samples. *Tectonophysics*, *475*, 327–358.

Zheng, Y. F., Fu, B., Gong, B., & Li, L. (2003). Stable isotope geochemistry of ultrahigh pressure metamorphic rocks from the Dabie-Sulu orogen in China: Implications for geodynamics and fluid regime. *Earth-Science Reviews*, *62*, 105–161.

Zheng, Y. F., & Hermann, J. (2014). Geochemistry of continental subduction-zone fluids. *Earth, Planets and Space*, *66*, 1–16.

Zheng, Y. F., Wu, Y. B., Chen, F. K., Gong, B., Li, L., & Zhao, Z. F. (2004). Zircon U-Pb and oxygen isotope evidence for a large-scale ^{18}O depletion event in igneous rocks during the Neoproterozoic. *Geochimica et Cosmochimica Acta*, *68*, 4145–4165.

Zheng, Y. F., Wu, Y. B., Zhao, Z. F., Zhang, S. B., Xu, P., & Wu, F. Y. (2005). Metamorphic effect on zircon Lu–Hf and U-Pb isotope systems in ultrahigh-pressure eclogite-facies metagranite and metabasite. *Earth and Planetary Science Letters*, *240*, 378–400.

Zheng, Y. F., Xia, Q. X., Chen, R. X., & Gao, X. Y. (2011). Partial melting, fluid supercriticality and element mobility in ultrahigh-pressure metamorphic rocks during continental collision. *Earth-Science Reviews*, *107*, 342–374.

Zheng, Y. F., Zhao, Z. F., Wu, Y. B., Zhang, S. B., Liu, X., & Wu, F. Y. (2006). Zircon U-Pb age, Hf and O isotope constraints on protolith origin of ultrahigh-pressure eclogite and gneiss in the Dabie orogen. *Chemical Geology*, *231*, 135–158.

Zong, K. Q., Liu, Y. S., Hu, Z. C., Kusky, T., Wang, D. B., Gao, C. G., … Wang, J. Q. (2010). Melting-induced fluid flow during exhumation of gneisses of the Sulu ultrahighpressure terrane. *Lithos*, *120*, 490–510.

SUPPORTING INFORMATION

Additional Supporting Information may be found online in the supporting information tab for this article.

How to cite this article: Wang S-J, Wang L, Brown M, et al. Fluid generation and evolution during exhumation of deeply subducted UHP continental crust: Petrogenesis of composite granite–quartz veins in the Sulu belt, China. *J Metamorph Geol*. 2017;35:601–629. https://doi.org.10.1111/jmg.12248